The Astronomical Journal, 171:126 (21pp), 2026 March https://doi.org/10.3847/1538-3881/ae2fc5

A Near-Earth Object Model Calibrated to Earth Impactors

Sophie E. Deam[1,2], Hadrien A. R. Devillepoix[1,2], David Nesvorný[3], Patrick M. Shober[4], Eleanor K. Sansom[2], Jim Albers[5], Eric Anderson[6], Zouhair Benkhaldoun[7,8,9], Peter G. Brown[10,11], Luke Daly[12,13,14], George DiBattista[6], Hasnaa Chennaoui Aoudjehane[15], Christopher D. K. Herd[16], Tom Herring[17], Jonathan Horner[18], Peter Jenniskens[19], Derek C. Poulton[6], Martin D. Suttle[20], and Anna Zappatini[21]

[1] Space Science and Technology Centre, Curtin University, GPO Box U1987, Perth, WA 6845, Australia; sophdeam@gmail.com
[2] International Centre for Radio Astronomy Research, Curtin University, GPO Box U1987, Perth, WA 6845, Australia
[3] Solar System Science & Exploration Division, Southwest Research Institute, 1301 Walnut St., Suite 400, Boulder, CO 80302, USA
[4] NASA Astromaterials Research and Exploration Science Division, Johnson Space Center, Houston, TX 77058, USA
[5] SETI Institute, 339 Bernardo Ave., Mountain View, CA 94043, USA
[6] Astronomical Society of Victoria, GPO Box 1059, Melbourne, VIC 3001, Australia
[7] Department of Applied Physics and Astronomy, and Sharjah Academy for Astronomy, Space Sciences and Technology, University of Sharjah, P.O. Box 27272, Sharjah, UAE
[8] High Energy Physics, Astrophysics and Geosciences Laboratory (LPHEAG), Faculty of Sciences Semlalia, Cadi Ayyad University, Marrakesh BP 2390, Morocco
[9] Oukaimeden Observatory, Cadi Ayyad University, 40273 Marrakesh, Morocco
[10] Department of Physics and Astronomy, University of Western Ontario, London, ON N6A 3K7, Canada
[11] Institute for Earth and Space Exploration, University of Western Ontario, London, ON N6A 5B8, Canada
[12] School of Geographical and Earth Sciences, University of Glasgow, Glasgow, G12 8QQ, UK
[13] Australian Centre for Microscopy and Microanalysis, The University of Sydney, Sydney, NSW 2006, Australia
[14] Department of Materials, University of Oxford, Oxford, OX1 3PH, UK
[15] GeoPen Laboratory, Faculty of Science Ain Chock, Hassan II University of Casablanca, km 8 Route d'El Jadida, Morocco
[16] Department of Earth and Atmospheric Sciences, 1-26 Earth Sciences Building, University of Alberta, Edmonton, AB T6G 2E3, Canada
[17] Jack C. Davis Observatory, Western Nevada College, 2269 Vanpatten Ave., Carson City, NV 89703, USA
[18] Centre for Astrophysics, University of Southern Queensland, West St., Toowoomba, QLD 4350, Australia
[19] SETI Institute, 339 Bernardo Ave., Mountain View, CA 94041, USA
[20] School of Physical Sciences, The Open University, Walton Hall, Milton Keynes, MK7 6AA, UK
[21] Institute of Geological Science, University of Bern, Baltzerstrasse 1+3, 3012 Bern, Switzerland
Received 2025 October 20; revised 2025 December 11; accepted 2025 December 14; published 2026 February 3

Abstract

The population of Earth-impacting meteoroids and their size-dependent orbital elements are key to understanding the origin of meteorites and informing planetary defense efforts. Outstanding questions include the role of collisions in depleting meteoroids on highly evolved orbits and the relative importance of delivery resonances. Those depend on size, with current dynamical models considering only asteroids larger than 10 m in diameter. Based on 1202 sporadic meteoroids observed by the Global Fireball Observatory, we created a debiased model of the near-Earth meteoroid population in the 10 g–150 kg size range (approximately 1 cm–0.5 m in diameter) as they dynamically evolved from the main asteroid belt onto Earth-crossing orbits. The observed impact population is best matched with a collisional half-life decreasing from 3 Myr for meteoroids of 0.6 kg (7 cm) or higher to 1 Myr below this size, extending to the model lower bound of 10 g. Placing our results in context with near-Earth object models for larger sizes, we find that the inner main belt continues to dominate feeding the small 1–10 m diameter population primarily via the ν_6 secular resonance and the 3:1J mean-motion resonance. We also evaluated the potential significance of physical processes other than collisions on Earth-impacting meteoroids, such as low-perihelion disruptions from thermal stresses.

Unified Astronomy Thesaurus concepts: Near-Earth objects (1092); Fireballs (538)

1. Introduction

Earth experiences a bombardment of interplanetary material as it orbits the Sun, from a continuous stream of dust particles micrometers to millimeters in size, through the less frequent interception of centimeter- to meter-sized meteoroids, to relatively rare encounters with >10 m diameter asteroids (G. O. Ryabova et al. 2019). As this material spans many orders of magnitude, it spans two important regimes: objects that are not easily detectable, and those that are hazardous. Such limitations and potential risk are a motivation to model the dynamics and evolution of material in the inner solar system.

Astronomers have been able to discover smaller and smaller near-Earth objects (NEOs) through decades of dedicated surveying. Here we consider any object with a perihelion distance $q < 1.3$ au to be an NEO; for an overview of NEOs in the context of other small bodies in the solar system, see J. Horner et al. (2020). Current estimates of the total number of expected NEOs indicate that we have discovered 90%–95% of objects with an absolute magnitude of $H < 17.75$ ($\gtrsim$1 km in diameter for an albedo of 0.14; A. W. Harris & P. W. Chodas 2021; D. Nesvorný et al. 2024b; R. Deienno et al. 2025). The discovery completeness estimates reduce significantly to only 26%–34% for NEOs with $H < 22.75$ (diameters approximately >100 m). Fortunately, new facilities and surveys such as the NEO Surveyor mission (A. K. Mainzer et al. 2023) and the Vera C. Rubin Observatory will discover many more small NEOs (J. A. Kurlander et al. 2025) and

improve the discovery completeness for such objects. NEOs observed with traditional telescopes are at their brightest and most observable when they are very close to Earth—especially if they are on a collision course with the Earth. Since the discovery of the first such imminent impactor, 2008 TC_3 (P. Jenniskens et al. 2009), there have been 11 instances of NEO discovery before impact (D. Farnocchia et al. 2016; P. Jenniskens et al. 2021; 2019 MO;[22] S. Geng et al. 2023; T. Kareta et al. 2024; P. Spurný et al. 2024; A. Egal et al. 2025; C. Ingebretsen et al. 2025; 2024 UQ;[23] F. Gianotto et al. 2025), which have all ranged between 0.5–10 m in size. That said, such objects can remain hidden in the Sun's glare and evade detection even during very close encounters, as was seen in the case of the 2013 Chelyabinsk impact (J. Borovička et al. 2013). This demonstrates that the meter-sized NEOs are the current lower limit for telescopic observability in asteroids.

Fortunately, NEOs become visible in the form of fireballs and meteors if they impact the Earth. Dedicated camera networks such as the Global Fireball Observatory (GFO; H. A. R. Devillepoix et al. 2020), European Fireball Network (J. Borovička et al. 2022), FRIPON (F. Colas et al. 2020), and the Global Meteor Network (D. Vida et al. 2021) have been recording the night sky for years to capture images of ablating interplanetary material.[24] These observatories can estimate the preimpact orbit and mass of a meteoroid, and measure its trajectory to predict a fall location in order to recover a meteorite. Since the impact frequency of meteoroids decreases with increasing size, these networks capture relatively few meteoroids $\geqslant$10 cm, instilling the need for long-duration, large-sky-area surveys such as the GFO to observe a significant number of such meteoroids. In contrast, telescopic surveys of NEOs are biased *against* the smallest objects in their observable range, and therefore record fewer observations of that end of the population, overall leading to the least amount of observations of NEOs 10 cm–10 m in size.

This scarcely observed population (10 cm–10 m) is critical because it covers the region across which objects become large enough to transition from being harmless spectacles to being potentially hazardous upon impact. Most authors typically consider the dividing line between those two regimes to lie around impact diameters of tens of meters (M. B. E. Boslough & D. A. Crawford 2008; B. M. Shustov et al. 2017; E. A. Silber et al. 2018; V. Svetsov et al. 2019). A specific example of an object that was large enough to be hazardous is the $\sim$19 m asteroid that fell over Chelyabinsk, producing an airburst containing an energy equivalent to about 500 kilotonnes of TNT (P. G. Brown et al. 2013; O. P. Popova et al. 2013), the shock wave from which shattered glass and injured many people. Impactors causing the scale of damage seen from the Chelyabinsk airburst are estimated to be relatively rare (N. Gi et al. 2018). This rarity, combined with the paucity of decameter-scale NEO observations, has led to an order-of-magnitude uncertainty in the estimated impact frequency of 10 m NEOs, from 2–3 yr up to 20–40 yr, as discussed in I. Chow & P. G. Brown (2025).

Understanding this population will also inform our understanding of meteorite delivery processes (J. Borovička et al. 2015). Meteorites tell us about the chemical makeup and formation processes of the terrestrial planets (T. H. Burbine & K. M. O'Brien 2004; L. Piani et al. 2020) and the composition of the solar system (B. Marty et al. 2024). Knowing the dynamic origin of such meteorites provides greater context to their previous passage through the solar system (e.g., A. J. King et al. 2022), to potentially link their composition and source asteroid family (R. P. Binzel et al. 2015; P. Jenniskens & H. A. R. Devillepoix 2025).

Much of our understanding of the evolution of NEOs larger than 10 m comes from models that trace an object's origin in the main asteroid belt and simulate its subsequent dynamical and physical evolution until the resulting population reproduces the observed characteristics. Many such models, from the innovative work of W. F. Bottke et al. (2002a) and S. Greenstreet et al. (2012) to the more recent models of M. Granvik et al. (2018) and D. Nesvorný et al. (2023; hereafter G18 and NEOMOD, respectively), to the subsequent NEOMOD2 and NEOMOD3 models (D. Nesvorný et al. 2024b, 2024c), and the most recent addition of R. Deienno et al. (2025), function in a similar way to each other, which we will describe here using the same notation and language as Table 1 in M. Granvik et al. (2018). Each model begins with a synthetic population of asteroids residing in the main belt or cometary reservoirs. Asteroid fragments, created through collisions (J. S. Dohnanyi 1969; D. D. Durda et al. 1998; W. F. Bottke et al. 2005b), evolve under nongravitational forces such as Yarkovsky drift and Yarkovsky–O'Keefe–Radzievskii–Paddack (YORP) evolution toward potential escape routes (P. Farinella et al. 1998; A. Morbidelli & B. Gladman 1998; W. F. Bottke et al. 2002b). Each of the models mentioned above mimics this process to varying degrees; NEOMOD simply places particles within a resonance with the same orbital distribution as asteroids neighboring the resonances, while G18 computes the drift of particles into the escape routes. Main-belt escape routes—which we will interchangeably call source regions—are locations within the belt where gravitational forces, such as the mean-motion and secular resonances with Jupiter and Saturn, respectively, perturb an asteroid's orbit and cause it to migrate from the main belt into near-Earth space ($q < 1.3$ au; G. W. Wetherill 1985; M. Granvik et al. 2017) and possibly onto Earth-crossing orbits. All of the above-mentioned models integrate particles under these gravitational perturbations through time to map each escape route to a subsequent distribution of time spent on particular orbits in near-Earth space, which we call residence time distributions, R_s. The models then combine the R_s to match debiased NEO observations and create a model NEO population. At this stage, the models represent only the dynamical evolution of NEOs, and subsequent differences to the observed population indicate where physical processes have modified the NEO population along its evolution.

A wealth of information about the physical processes acting on NEOs >10 m has been extracted and refined using these models. First of all, the main-belt sampling of escape routes was found to be size dependent (M. Granvik et al. 2018). Second, as initially shown by M. Granvik et al. (2016), asteroids that pass close to the Sun appear to completely disrupt. The removal of low-q particles was implemented in the G18 and NEOMOD models to produce a better match

[22] https://minorplanetcenter.net/mpec/K19/K19M72.html

[23] https://minorplanetcenter.net/mpec/K24/K24U49.html

[24] A detailed description and historical overview of all networks of meteor cameras worldwide is beyond the scope of this work; for such an overview, we direct the interested reader to P. Jenniskens & H. A. R. Devillepoix (2025) and references therein.

between the main-belt-derived distributions and the NEO population. The authors also found that the disruption distance is size dependent. Extrapolation of the size–distance relation of M. Granvik et al. (2016) to objects of 1 m in diameter implies a disruption distance of $q = 0.4$ au. It has not been directly tested whether this phenomenon also effects meteoroids of this size, though fireball observations do show a paucity at such perihelia (P. Wiegert et al. 2020). Finally, M. Granvik & K. J. Walsh (2024) identified a NEO source from around the Earth and Venus created by tidally disrupted material.

The extrapolation of these size-dependent features or the introduction of new processes to smaller meteoroid sizes is an important step toward understanding the hazardous and meteorite feeding population. For example, NEOs that have recently evolved from the belt can still collide with main-belt asteroids while their aphelion remains inside the belt ($Q > 1.8$ au; D. Nesvorný et al. 2024b). Collisions are therefore a dominant, strongly size-dependent driver of the main belt and near-Earth asteroid populations (W. F. Bottke et al. 2005a). For main-belt fragments 1–10 cm in size, modern collisional-evolution models yield mean catastrophic lifetimes of ~3–6 Myr (W. F. Bottke et al. 2005b; G. C. de Elía & A. Brunini 2007; see also P. Farinella et al. 1998). Because NEOs encounter the main-belt fragments at higher relative velocities (≈8–11 km s^{-1} instead of ≈5 km s^{-1}), their collisional lifetimes are shortened by roughly a factor of 3 to 1–3 Myr for the same size range. This estimate agrees with dynamical fits to the orbital distribution of fireballs (A. Morbidelli & B. Gladman 1998), and is broadly consistent with more recent Öpik-based calculations that find lifetimes of 5–10 Myr for 1–10 m-sized NEOs (D. Nesvorný et al. 2024b).

Another size-dependent feature to consider is the orbital inclination distribution of asteroids within the main belt. The initial particle distributions used in the G18 and NEOMOD simulations were designed to mimic the inclinations of the currently observed (>100 m) main-belt asteroids. However, much of the smaller asteroidal debris is not expected to follow this same distribution. Younger asteroid families still contain large numbers of small fragments that have yet to disperse through Yarkovsky drift (W. F. Bottke et al. 2006), keeping them dynamically concentrated and actively undergoing collisional cascades. Several of these families are also associated with zodiacal dust bands—for example, the Veritas and Karin families—indicating that they produce debris down to micrometeoroid sizes (D. Nesvorný et al. 2006). Many such young families, including Massalia, Karin, Koronis, and Themis, have low orbital inclinations (D. Nesvorný et al. 2024a), where small meteoroids originating from them would share similarly low-inclination orbits before escaping the main belt. As a result, the orbital evolution of small meteoroids in near-Earth space per source region may differ from that of the larger asteroids used in previous models.

Investigating the hazardous decameter NEOs can be accomplished by studying objects both an order of magnitude smaller and larger in diameter and inferring the size-dependent characteristics between the populations. The NEOMOD models extend to an absolute magnitude as high as $H = 28$, or NEOs ≈10 m. In this paper, we present a model for smaller objects. We use meteoroid observations from the GFO to analyze size-dependent main-belt migration and physical processing for meteoroids of sizes approximately 1 cm–0.5 m.

We make the assumption that all of our observed meteoroids were liberated from their parent bodies while residing in the main asteroid belt. Several mechanisms exist which remove meteoroids from a body in near-Earth space, such as sublimation-driven activity (D. Jewitt 2012), collisions and cratering (W. F. Bottke et al. 2025c), thermal fatigue or rotational breakup from close encounters with the Sun (M. Granvik et al. 2016), and tidal forces during close approaches with the terrestrial planets (E. Schunová et al. 2014; M. Granvik & K. J. Walsh 2024)—the latter of which is known to contribute to the $H < 25$ NEO population. We do not expect any of these sources to be a major contribution to the meteorite-precursor population that we model. This is because bodies in near-Earth space only remain on such orbits for on average <10 Myr (B. J. Gladman et al. 1997; M. Granvik et al. 2018), while the cosmic-ray exposure (CRE) ages of meteorites, which measure how long material has been isolated to a body <2 m in diameter, are generally much longer than these short dynamical lifetimes (K. Marti & T. Graf 1992; O. Eugster 2003). This implies that most meteorites must be liberated from parent bodies in the main asteroid belt, where delivery timescales match the measured CRE ages (A. Morbidelli & B. Gladman 1998). An exception is the rare CI/CM chondrites, whose short CRE ages (mostly <2 Myr) require an alternative delivery mechanism. CI/CM chondrites, however, make up <2% of falls.[25] Like the first debiased NEO model of W. F. Bottke et al. (2002a), which incorporated only 138 NEOs, our study relies on relatively few observations, particularly at larger sizes, with ~200 meteoroids ≳10 cm in diameter. Thus, we restrict our modeling to the dominant evolutionary pathway for meteorite precursors and do not attempt to include alternative sources.

The paper is structured as follows. Section 2 introduces the GFO dataset, the meteoroid selection criteria, and debiasing techniques. Section 3 describes the parameter fitting routines to create the NEO model. In Section 4, we evaluate the model's performance and limitations. Finally, we relate back to the meteoroid population in Section 5.

2. Data: Earth Impactors and Debiasing

The GFO (H. A. R. Devillepoix et al. 2020) is an international collaborative project, born from the original efforts of the Australian Desert Fireball Network (P. A. Bland et al. 2012) to image bright fireballs and recover meteorites using long-exposure digital images from a distributed network of cameras. The data that we use in this study were captured over several iterations of camera hardware (R. M. Howie et al. 2017a, 2017b). Images are astrometrically calibrated (H. A. R. Devillepoix et al. 2018), and the fireballs captured within them are detected (M. C. Towner et al. 2020), triangulated using the straight-line least-squares method (J. Borovička 1990), and dynamically modeled using an extended Kalman filter (E. K. Sansom et al. 2015). The preimpact orbit and its uncertainty is determined by sampling within the measurement error of the highest recorded velocity vector with a Monte Carlo approach to create 1000 clones (T. Jansen-Sturgeon et al. 2019). The clones are individually propagated backward to a position outside the sphere of Earth's influence and converted into heliocentric orbital elements, where the mean and 1σ value in each orbital-

[25] The Meteoritical Bulletin (www.lpi.usra.edu/meteor/).

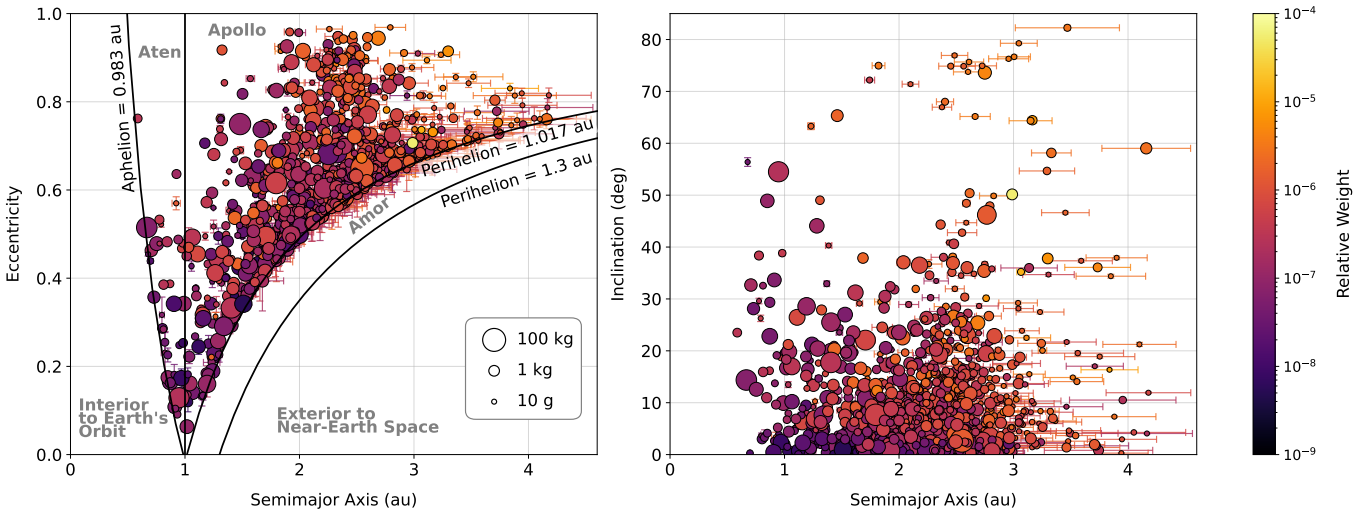

Figure 1. The GFO observed meteoroids used as calibration data plotted by their semimajor axis, eccentricity, and inclination. The sizes represent their masses at the top of the atmosphere, and the colors represent their relative weighting used for debiasing, derived from their Earth-impact probability and detectability as a function of mass and speed.

element distribution provides the final orbit and uncertainty. Since the data collection began in 2014, upwards of 2000 fireballs have been detected and triangulated over 10 yr.

To create a debiased model of the centimeter- to meter-sized NEO population, we selected fireball events for the calibration dataset. The quality cuts and selection criteria included high-quality observing geometry, lower limits on the meteoroid's initial mass, and no association with a known meteor shower (see Appendix A). At the end of this process, we were left with 1202 sporadic meteoroids captured between 2014 and 2024.

Figure 1 shows the debiased fireball data after the appropriate weightings were applied (see Appendix B for debiasing methodology) and the data were normalized to 1202, the effective number of meteoroids they represent. The slope of the size–frequency distribution of the debiased meteoroids follows a broken power law, very similar to that measured in the debiased fireball survey of I. Halliday et al. (1996), covering the same size range as our data. For GFO meteoroids with masses M above 2.0 ± 0.5 kg, we measure the cumulative number N as $\log(N) \propto -1.059\log(M)$. This matches, within reason, to the constant power law of the extrapolated main asteroid belt and NEO population for asteroids with scale-free disruption laws under collisional equilibrium (J. S. Dohnanyi 1969, slope −1.167; D. P. O'Brien & R. Greenberg 2003, slope −1.2), that of bolides (P. Brown et al. 2002, slope −0.90), and that of fireballs (I. Halliday et al. 1996, slope −1.06).

3. Methods: Model Building

Following the approach of previous NEO models (that of W. F. Bottke et al. 2002a, G18, and NEOMOD), we have fit a maximum-likelihood function between our debiased orbital data and distributions of simulated NEOs originating from either the main asteroid belt or Jupiter-family comet (JFC) region. The aim of the model is to determine the relative flux of each NEO source required to reproduce the true orbital distribution of NEOs. We describe below where our methodology is tailored toward the meteoroid population, with the remaining details of the statistical framework and parameter fitting routine discussed in Appendix C.

3.1. Data Binning

The model calibration data were distributed into cells according to the meteoroid size and orbital elements: semimajor axis a, eccentricity e, and inclination i (Table 1). These bin sizes encompass the orbital uncertainties of the fireballs, which are typically less than 0.1 au, 0.02, and $0.^{\circ}5$ for a, e, and i, respectively (see Figure 1), but do increase for higher semimajor axis orbits because of the greater speeds with which they impact the Earth (see Section 2 for more information on calculating meteoroid orbits from fireball observations). This created a four-dimensional distribution $N_{\rm GFO}(a,\ e,\ i,\ H)$ containing $21 \times 12 \times 15 \times 28 = 105{,}840$ cells. The absolute magnitude axis, H, was used as a proxy for meteoroid size. This was chosen so that the model works at the same scale, $\propto \log(m^{1/3})$, as other NEO models using telescopic survey data, which intrinsically measure H. The meteoroid entry mass calculated by the GFO pipeline was transformed into H, assuming a density of 3500 kg m^{-3} and geometric albedo of 0.147 (typical values for an ordinary chondrite). Ideally, one would want to develop a model using a directly observed measure of size such as mass, diameter, or cross-sectional area. In the case of fireballs, however, we do not directly observe any of those quantities without making some assumption about the meteoroid's physical properties. Hence, using H as a proxy for size in the model is no worse than the alternatives; we will convert between H, mass, and diameter for the purpose of discussion throughout the paper, using the assumed quantities stated above. To assess whether converting from mass to H without knowing individual meteoroid properties significantly impacts the model fit or interpretation, we consider the conversion across various meteorite types. The meteorites types most visibly distinct from ordinary chondrites are aubrites and eucrites, which are associated with bright E-/Xe- and V-type asteroids, respectively. Using nominal albedo and bulk densities (R. J. Macke et al. 2011; F. Usui et al. 2013), the difference in H, for any mass, between an ordinary chondrite and an aubrite or eucrite is −2.0 or −1.8, respectively. This is significant compared to the H bin size; however, the model flexibility along the H-axis is constrained to at maximum three steps which are at least $\Delta H = 2$ apart.

Table 1
The Cells Used to Divide the Model Calibration Data (the GFO Meteoroids) and Residence Time Distributions

Dimension	Range	Step Size
a (au)	0–4.2	0.2
e	0.04–1.00	0.08
i (deg)	0–60	4
H	34.5–41.5	0.25

Additionally, these meteoroid types are not significant among NEOs (M. Marsset et al. 2022) or meteorites,[26] and thus we expect no more than 5% of the 1202 meteoroids in our dataset to have a greatly overestimated H, i.e., they should be in much "brighter" H bins. The second most common meteoroid type we expect after ordinary chondrites, carbonaceous chondrites, have a nominal ΔH of -0.8. A reasonable portion of our data (somewhere between 4% and ∼32% based on meteorite falls and NEO statistics; M. Marsset et al. 2022) will have H underestimated by at maximum three bins. We would not expect these shifts to alter the calibration data enough to create significantly different model results, as the uncertainties on the final posterior distributions of the free parameters as they stand are rather large.

3.2. Residence Time Distributions $\mathrm{R_s}$

We call the distribution of orbits originating from a source s the residence time distribution, R_s, which is a function of (a, e, i). We use the same as those created for the NEOMOD models (D. Nesvorný et al. 2023), to which we direct the reader for a full description of their derivation, but describe briefly below. Eleven residence time distributions were created by populating the resonance gaps in the main asteroid belt with massless test particles and tracking their motion within near-Earth space ($q < 1.3$ au) during 500 Myr numerical integrations of the solar system. The particles' initial locations within the mean-motion resonances with Jupiter (3:1, 5:2, 7:3, 8:3, 9:4, 11:5, and 2:1), and the secular resonance with Saturn (ν_6), were distributed bordering the resonance gaps according to the trends of main-belt asteroids (>100 m in size). The initial positions for the Hungaria population, Phocaeas population, and the particles expected to evolve along weak inner resonances ($2.1 < a < 2.5$ au, $i < 18°$, $q > 1.66$ au) were taken from real asteroid positions in the respective populations. The time the particles spent with certain (a, e, i) after being perturbed from the main belt and reaching near-Earth space was recorded and averaged to create the residence time distributions as a function of those orbital elements, $R_s(a, e, i)$. The 12th and final R_s, representing the JFC population, was developed in D. Nesvorný et al. (2017).

When we produced the R_s to account for physical processes in the inner solar system (see Section 3.3), the finite number of particles in the original orbital integrations resulted in many empty bins. To accommodate this, the resolution of the 12 new R_s were reduced from that used in NEOMOD to the resolution outlined in Table 1. Namely, the bin widths along the semimajor axis and eccentricity were doubled, and the inclination range was reduced to below 60°. We also uniformly filled any empty bins with a small flux of $1e^{-8}$, which is at the tail end of the flux distribution of the filled bins, and renormalized R_s to 1 again. This downsampling and bin filling allowed for smooth log-likelihood calculations with minimal influence on the final model fit.

3.3. Meteoroid Residence Time Distributions

We now introduce a range of meteoroid specific R_s distributions. These were created as the initial model fits using the NEOMOD R_s matched the GFO meteoroid distribution poorly. This is not surprising, as the NEOMOD R_s were created from orbital simulations designed to replicate the passage of decameter to kilometer asteroids from the main belt. The additional R_s, described below, replicate the physical effects applicable to smaller asteroids as they evolve from the main belt.

3.3.1. Collisions $\mathrm{R_{s,\mathit{Myr}}}$

Asteroids in the main asteroid belt are subject to disruption from a collision with another asteroid, and near-Earth asteroids are no exception. The collisional lifetimes of large near-Earth asteroids are typically longer than the relatively short dynamical lifetimes of objects within the inner solar system, so there has been no need to include them in previous NEO models (discussed in Section 7.6 of D. Nesvorný et al. 2024b). As we are modeling meteoroids with diameters of less than 1 m, however, the expected collisional lifetimes are now on the order of or less than the dynamical lifetimes, altering the expected orbital distribution of such a near-Earth meteoroid population. We mimicked collisions in the numerical integrations to produce *collisionally evolved* R_s distributions. For each particle, the probability of a collision P_{col} was modeled by an exponential cumulative distribution function, $P_{\mathrm{col}} = 1 - e^{h/t_{\mathrm{col}}}$, for the simulation interval $h = 1000$ yr. When $P_{\mathrm{col}} < x$ for some randomly generated value $0 < x < 1$, the particle was removed from the simulation. This was calculated at each simulation interval for particles with an aphelion of $Q > 1.8$ au still coupled to the main asteroid belt, where collisions are estimated to occur with the half-life of t_{col}. This aphelion condition was also adopted by A. Morbidelli & B. Gladman (1998) in their analysis of the collisional lifetimes of decimeter NEOs, as it represents only collisions between NEOs and the comparatively concentrated main-belt asteroid population. We also tested collisions without any condition on Q for comparison; however, the aphelion condition was preferred by the model and is used throughout the rest of the modeling procedure.

The most appropriate collisional lifetime to include depends on the size of the objects being investigated (introduced in Section 1). The sizes of the GFO meteoroids used to calibrate this model are approximately 1 cm to 0.5 m in diameter, so we created R_s distributions of NEOs with $t_{\mathrm{col}} = 3$ Myr, 1 Myr, and 0.5 Myr. As only the residence time distributions with mean dynamical lifetimes equal to or shorter than t_{col} are significantly influenced by collisions, for $t_{\mathrm{col}} = 3$ Myr we created $R_{s,3\mathrm{Myr}}$ only for the ν_6 and inner weak sources. Without introducing any depletion (e.g., collisions or low-q disruptions), R_{ν_6} and R_{Inner} have mean dynamical lifetimes of 9.5 Myr and 7.0 Myr, respectively, while the rest of the sources employed in the model have much shorter dynamical lifetimes on the order of 1 Myr or less.[27] In our 3 Myr collisional models, we used $R_{\nu_6,3\mathrm{Myr}}$ and $R_{\mathrm{Inner},3\mathrm{Myr}}$ along with the

[26] The Meteoritical Bulletin (www.lpi.usra.edu/meteor/).

[27] The mean dynamical lifetimes of the base R_s differ from the R_s with low-perihelion disruptions as reported in Table 5 of D. Nesvorný et al. (2023). R_s without low-perihelion disruptions have longer mean dynamical lifetimes.

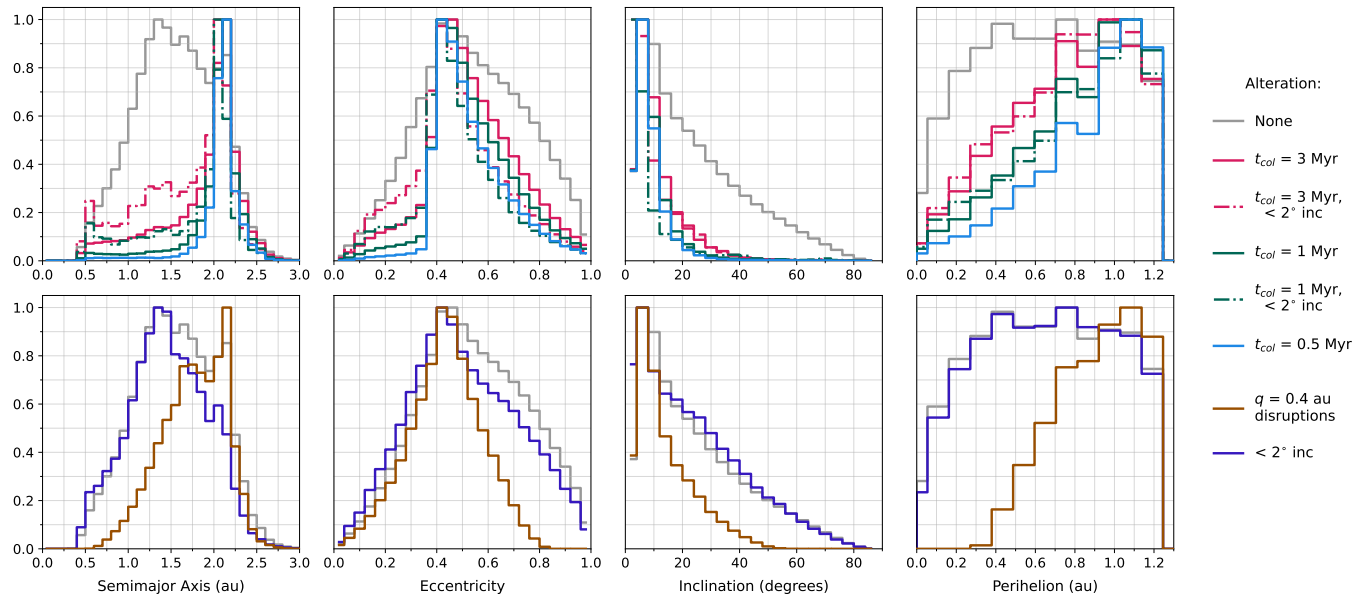

Figure 2. A comparison of orbital distributions for particles that have escaped from the ν_6 resonance and evolved under various physical processes. The top panel shows the result for simulations including different collisional lifetimes (t_{col}), while the bottom panel shows the output of low-perihelion ($q < 0.4$ au) disruptions or main-belt asteroids restricted to low (<2°) inclinations. The top panel also shows the combination of collisions and low inclination input with the dotted–dashed line. The simulation which created these distributions was integrated initially for 100 Myr to capture particle escape from the main belt, and a further 400 Myr for particles within $q < 1.3$ au to track further evolution (see D. Nesvorný et al. 2023 for further details).

NEOMOD R_s for the other sources. We created R_s with t_{col} = 1 Myr and 0.5 Myr for all 12 sources.

Figure 2 shows an example of the meteoroid R_s for the ν_6 source region. The dominant trend for the collisionally evolved R_s is a decreasing contribution from particles on highly evolved orbits with decreasing collisional lifetime. This is shown by a significantly reduced signal from semimajor axis values <1.6 au. The eccentricity peak at 0.44 is also narrower, and the inclination distribution changes from a gradual decrease from the ecliptic toward 90° to a sharp peak at 8°, followed by a sudden decay to very little signal for orbits with inclinations >40°. The perihelion distribution also shifted from a flat distribution ranging from 0 to 1 au to an increasing slope peaking at 1 au.

3.3.2. Low-perihelion Disruption $R_{s,0.4au}$

We created R_s including catastrophic disruptions for particles with $q \leqslant 0.4$ au. If meteoroids were to disrupt near the Sun in the same way as larger asteroids, then we would not expect them to survive within about 0.4 au. This distance corresponds to extrapolating the disruption law of M. Granvik et al. (2016) down to objects of 1 m in diameter. Such disruption was invoked by monitoring each simulated particle's perihelion distance and removing it when it reached $q \leqslant 0.4$ au for the first time. This primarily removes highly eccentric orbits (Figure 2). Other prominent features are a swap in the semimajor axis peak from ∼1.2 au to ∼2.1 au, a sharpening of the eccentricity peak at 0.4, a decrease in high-inclination orbits, and a removal of low-perihelion orbits to create a steep slope from 0.4 to 1 au.

3.3.3. Isolating Low-inclination Sources $R_{s,\circ}$

In the final set of meteoroid R_s distributions, we restricted the simulation input to low-inclination particles. This was intended to mimic young asteroid families, which are often located at low inclinations and predominantly feed neighboring main-belt escape regions due to their greater amount of small debris (see M. Brož et al. 2024a and references therein). We restricted the input particles for $R_{\nu 6}$, $R_{3:1J}$, $R_{2:1J}$ to those below 2°, 2°, and 5°, respectively. It is worth noting that the particles below these inclinations still follow the same input distributions originally developed for NEOMOD, which were derived from the positions of the largest asteroids in the main belt. This created subtle differences for $R_{\nu_6,2^\circ}$ (Figure 2), the most significant being the reduction of the second semimajor axis peak at 2.2 au.

4. Model Fitting and Results

With both the NEOMOD residence time distributions and the new meteoroid-appropriate residence time distributions (R_s and $R_{s,\mathrm{Myr}}$, $R_{s,0.4\mathrm{au}}$, $R_{s,\circ}$, respectively), we followed the methods of NEOMOD and fit such distributions to the calibration fireballs using a maximum-likelihood estimate according to Equations (C1)–(C8) in Appendix C to find the optimal number of sources n, strength parameters α_s per source as a function of size, number of linear segments, or "slopes," m that $\alpha_s(H)$ is divided into to create the model flexibility with size, and crossover index δ, which describes the transition between the types of R_s along the H-axis.

4.1. Best-fitting Model

The optimal number of sources to include in the model was $n = 6$, including inner weak, ν_6, 3:1J, 5:2J, 2:1J, and JFC. We tested this by adding the asteroidal R_s (without any physical processes, using $m = 3$) incrementally to the model until the highest log-likelihood value was reached (Figure 3). One inner-belt source and one outer-belt source, $R_{3:1J}$ and $R_{5:2J}$, were used as the starting input, from which the remaining sources were added. `multinest` penalizes models with too many parameters to prevent overfitting, which is why a

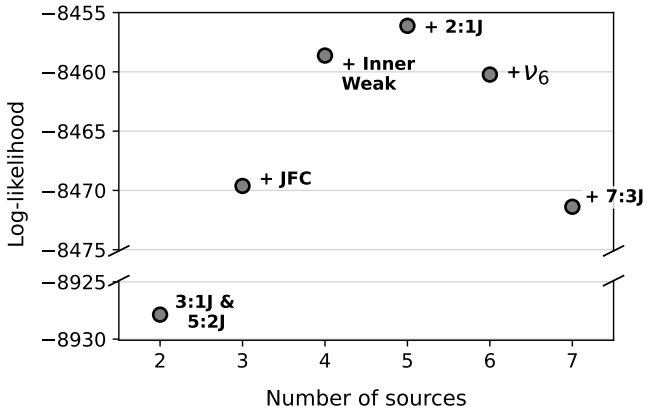

Figure 3. The log-likelihood values of the best-performing source-region combinations in a three-slope model. The log-likelihood has the highest value for the five sources 3:1J, 5:2J, inner weak, JFC, and 2:1J. The addition of more sources decreases the log-likelihood, only marginally for the 6th (ν_6) but more significantly for the 7th (7:3J).

turnover is seen in the log-likelihood for more than five sources. We decided a six-source model was the most appropriate, even though five sources produced the highest log-likelihood. This is because $R_{\nu 6}$ and $R_{3:1J}$ are very similar, so the degeneracy between them is important to evaluate. Also, the difference in log-likelihood between four, five, and six sources is small, with Bayes factors ($\Delta\mathcal{L}$) of <5. When a 7th source was added, the best-performing additional source was 7:3J; however, `multinest` allocated that source 0% contribution, i.e., $\alpha_{7:3J}(H) = 0$. This indicates that the calibration dataset cannot distinguish between any more sources, and from this we are certain these six sources are sufficient to describe the general trends of the centimeter-to-meter NEO population.

The best-performing number of slopes in the strength function (Equation (C1)) for this dataset was $m = 3$. We computed model fits with m ranging from 1 to 4. The log-likelihood continued to increase with increasing numbers of slopes and freedom given to the model. We therefore relied on physical intuition to determine that one or two slopes provided insufficient flexibility along the H-axis, and that four slopes produced rapid oscillations between sources for different sizes, indicating that the model was overfitting to the data. Three slopes created a smooth transition between sources and were the most appropriate for describing general trends in the data without overfitting.

The best-performing meteoroid R_s had collisions for lifetimes of 3 Myr and 1 Myr. Compared to the models using the asteroidal R_s, these models have Bayes factors of 144 and 63, respectively. What became clear from investigating the model performance across distinct size ranges (Figure 4) is that 3 Myr dominates at largest sizes while 1 Myr dominates at smaller sizes. This was confirmed by fitting a model with both $R_{s,3\mathrm{Myr}}$ and $R_{s,1\mathrm{Myr}}$, and `multinest` fitting the crossover at $\delta = 38.5$ (∼0.6 kg). This crossover model has a Bayes factor of 190 compared to a model with just the original R_s. Figure 4 also shows that the model including low-inclination inputs alongside collisions yields comparable performance to the collision-only model. However, we chose to adopt the collisions-only model moving forward for several reasons. First, the R_s distributions incorporating the combined physical processes contained the most empty bins (see Section 3.3). Second, the restriction to low inclinations provides only a simple approximation of the true spatial distribution of small main-belt asteroids. Finally, the differences in performance and output distributions between the two model types are only minor. Given the performance of the model with these limitations, we demonstrate a strong case for future exploration of this framework. Overall, we choose the crossover model transitioning from 3 Myr collisions to 1 Myr at around ∼0.6 kg as our best description of the centimeter-to-meter NEO population.

The contributions from the sources for the best-fitting model, as determined by `multinest`, are displayed in Table 2 and shown in Figure 5, along with the corresponding 1σ uncertainties. The largest sizes probed by this model, 10–150 kg, are supplied by a combination of the inner weak, ν_6, 3:1J, and 5:2J sources. Looking across the entire size distribution, the ν_6 contribution stays relatively constant, while the contributions from the inner weak, 5:2J, and 2:1J sources decrease with size. Interestingly, the 3:1J source peaks around 0.25 kg, with approximately a 50% contribution, the next-greatest contribution at this size being $\nu_6 \sim 20\%$. The smallest size range, 10–250 g, is reproduced by JFC-type orbits as it has the greatest contribution at 50%, with <10% contribution from the inner weak, 5:2J, and 2:1J sources, and around 20% from both ν_6 and 3:1J. In summary, we have found the relative contributions of the dominant main-belt sources feeding the centimeter-to-meter NEO population.

The α-parameter uncertainties are the greatest at the largest model sizes because of the smaller number of fireballs used to calibrate the model and the degenerate nature of the inner main-belt sources. Figure 6 shows examples of the marginal posterior distributions (full plot in Appendix D). The parameters for the largest sizes, $\alpha_{s,1}$, show major degeneracy for the sources ν_6, inner weak, 3:1J, and 5:2J, while 2:1J and JFC appear independent. Unfortunately, we do not have enough data in this size region to constrain each inner-belt source individually. A further complication is that, while each individual sample of `multinest` fulfils $\sum_{s=1}^{n} \alpha_s = 1$, the median values of each posterior distribution do not always sum to 1, so we use the normalized values (bracketed column in Table 2) when comparing source-region contributions. We demonstrate that the best-fitting model is robust, i.e., is not fitting to specific data points, by dividing the calibration dataset in half and refitting our $s = 6$, $m = 3$ model (Appendix E) and seeing that the relative strengths of the source regions do not change significantly.

4.2. Evaluation of Fit

The best-fit model comprehensively matches the debiased fireball population. To compare the two distributions, 200 model outputs were created by taking a set of the $\alpha_{s,m+1}$ parameters from within the `multinest` marginal posterior distributions. These α parameters all fall within the 1σ uncertainties reported in Table 2 and combine to create models of comparable performance to the best-fit combination (Bayes factors of <2). Using parameters from the marginal posterior distribution ensures the degeneracy between the source-region strength is preserved in each model created, and the parameter 1σ uncertainties are sampled effectively. For each combination, we used $t_1 = 3$ Myr, $t_2 = 1$ Myr, and $\delta = 38.5$ in Equation (C4) to create $N(a, e, i, H)$. Each $N(a, e, i, H)$ was reduced in H range and sampled the same

Table 2
The Parameters for the Strength Function, $\alpha_{s,m+1}$ for the Best-fitting Model

Source	α_1	α_2	α_3	α_4	$\sigma(\alpha_1)$		$\sigma(\alpha_2)$		$\sigma(\alpha_3)$		$\sigma(\alpha_4)$	
ν_6	0.203 (0.235)	0.332	0.207	0.264	0.075	0.394	0.272	0.395	0.177	0.239	0.228	0.301
Inner weak	0.143 (0.166)	0.033	0.008	0.02	0.050	0.304	0.009	0.077	0.002	0.019	0.006	0.045
3:1J	0.285 (0.330)	0.158	0.512	0.177	0.128	0.489	0.087	0.241	0.473	0.553	0.139	0.217
5:2J	0.145 (0.168)	0.192	0.082	0.025	0.05	0.299	0.112	0.282	0.053	0.115	0.008	0.048
2:1J	0.042 (0.049)	0.104	0.043	0.007	0.013	0.102	0.061	0.148	0.026	0.061	0.002	0.016
JFC	0.045 (0.052)	0.156	0.141	0.496	0.013	0.108	0.097	0.221	0.111	0.171	0.465	0.528

Note. α_1 and α_4 are the outer bounds of the model at $H = 34.5$ and 41.5, and α_2 and α_3 are anchor points defining the breaks in the slope at $H = 36.75$ and 39.25, respectively. The crossover from a collisional lifetime of 3 Myr to 1 Myr is between $\alpha 2$ and $\alpha 3$ at $H = 38.5$ (about 0.6 kg). The values shown are the medians and 1σ bounds of the marginal posterior distributions. As each parameter may be drawn from a nonnormal distribution and normalization to 1 applies only to each posterior draw, the medians of the marginals do not always sum to 1; the normalized value is provided in brackets where it differed significantly.

number of times as the number of meteoroids within that size range of the GFO calibration dataset to create an equivalent resolution distribution for comparison. Finally, to change $N(a, e, i, H)$ from the model resolution (Table 1) to a continuous distribution, (a, e, i) was randomly resampled within each bin range. We extract the median and various percentiles of the orbital-element distributions from the 200 model outputs for comparison against the weighted GFO calibration data in Figure 7. The general trends of each size range are well matched by the model outputs, particularly the reduction in flux at a semimajor axis of 1 au for decreasing sizes, and the narrowing of the eccentricity peak. We show the distribution of the $H = 36.5$–38.5 range both with and without one strongly weighted, high-inclination meteoroid, which was used in the calibration dataset. Note that the inclusion or exclusion of this event from the model fitting did not change which model performed best, nor the resulting α parameters. The mismatch at the smallest sizes is a curiosity, as it is not likely a result of a small quantity of data. For $H = 38.5$–40, the model's semimajor axis distribution peaks above the GFO data at 2.6 au, while the eccentricity shows excellent agreement. In contrast, for $H = 40$–41.5, the model's eccentricity peaks above the data at 0.75, while the semimajor axis aligns well.

This could be explained by a consistent peak at a perihelion of 1 au in the meteoroid data, not present in the model output, for data $H > 36.5$ (Figure 7 (b)). There is also a spike at $q = 0.4$ au for the largest objects, but this is an artifact of the small number of meteoroids in this size range. As our calibration data are made up of only Earth impactors (the majority of which have perihelion values of $q = 1$ au), it is difficult to know, despite our debiasing procedures, whether or not we have created a true representation of near-Earth meteoroids to compare to main-belt-derived material. Overall, the strong match in the semimajor axis distribution between the debiased meteoroids and the model output gives strong support for the inclusion of collisions in the centimeter- to meter-sized NEOs, a reduction in collisional lifetime as sizes decrease, and the use of this model to represent the meteoroid population.

5. Model Interpretation and Discussion

5.1. Inner-belt Dominance

Placing our results in the context of meteoroid delivery to the inner solar system, we can reaffirm the dominance of the inner belt feeding the near-Earth region through the ν_6 and 3:1J resonances. The parameters $\alpha_s(H = 34.5)$ and $\alpha_s(H = 39.75)$ for the inner weak, ν_6, and 3:1J sources show that our model predicts a decreasing, 73% to 53% contribution from the inner-belt sources over the size range 150 kg to 6 kg (approximately 0.5 m to 15 cm in diameter, assuming a density of 3500 kg m^{-3}). These parameters, however, are correlated with those of the 5:2J resonance (see Appendix D), which have median values 16%–19% over this size range. Only an increase in the number of observed fireballs over this size range could resolve the degeneracy between sources. Compared with predictions from other NEO models, our inner-belt contribution is generally smaller, though consistent within uncertainties. NEOMOD2 predicts 91% of $H = 28$ (10 m diameter for an albedo of $p_v = 0.14$) NEOs originate from the ν_6 and 3:1J resonances alone (inner weak <1%). R. Deienno et al. (2025) estimate a 77% contribution from ν_6 and 3:1J and 11% from the inner weak resonances, predicting an 88% dominance from the inner main belt. Returning to submeter sizes, A. Morbidelli & B. Gladman (1998) proposed that Earth-impacting meteoroids can be fed primarily by the ν_6 and 3:1J resonances in roughly equal proportions, which we agree with despite subtle differences in the dataset and methods. Their analysis used 63 fireballs with initial masses ranging from 30 g to 25 kg. While this matches the mass range of our calibration meteoroids, the authors only analyzed potential meteorite-dropping fireballs, whereas we were inclusive of any meteorite fall potential. They also used an Öpik-style impact probability calculation that has been shown to produce unexpected population analyses (e.g., calculating the ratio of afternoon to morning meteorite falls, the PM ratio; J. Wisdom 2020). Overall, our model reinforces the notion of inner-belt dominance across the extended size range of hundreds-of-meter- to centimeter-diameter NEOs.

The generally agreed upon explanation for the inner-belt dominance for subkilometer asteroids is the greater mobility of material in the main asteroid belt and strength of these escape routes. The primary mechanism for this mobility is the Yarkovsky effect, a thermophysical effect producing a net force either inwards or outwards from the Sun for prograde or retrograde rotating asteroids, respectively (P. Farinella et al. 1998; A. Morbidelli & B. Gladman 1998; W. F. Bottke et al. 2002b). The magnitude of the effect depends on the asteroid's size, distance from the Sun, and physical properties of the body. The change in semimajor axis over time for a 1 m diameter body in the main belt ranges from 0.001 to 0.01 au Myr^{-1} (W. F. Bottke et al. 2002b, 2006). This drift rate causes asteroids to "jump" across weak resonances until they reach the stronger ν_6 and 3:1J regions, which are very efficient at evolving asteroids onto Earth-crossing orbits in comparison to outer-belt resonances—with a factor of

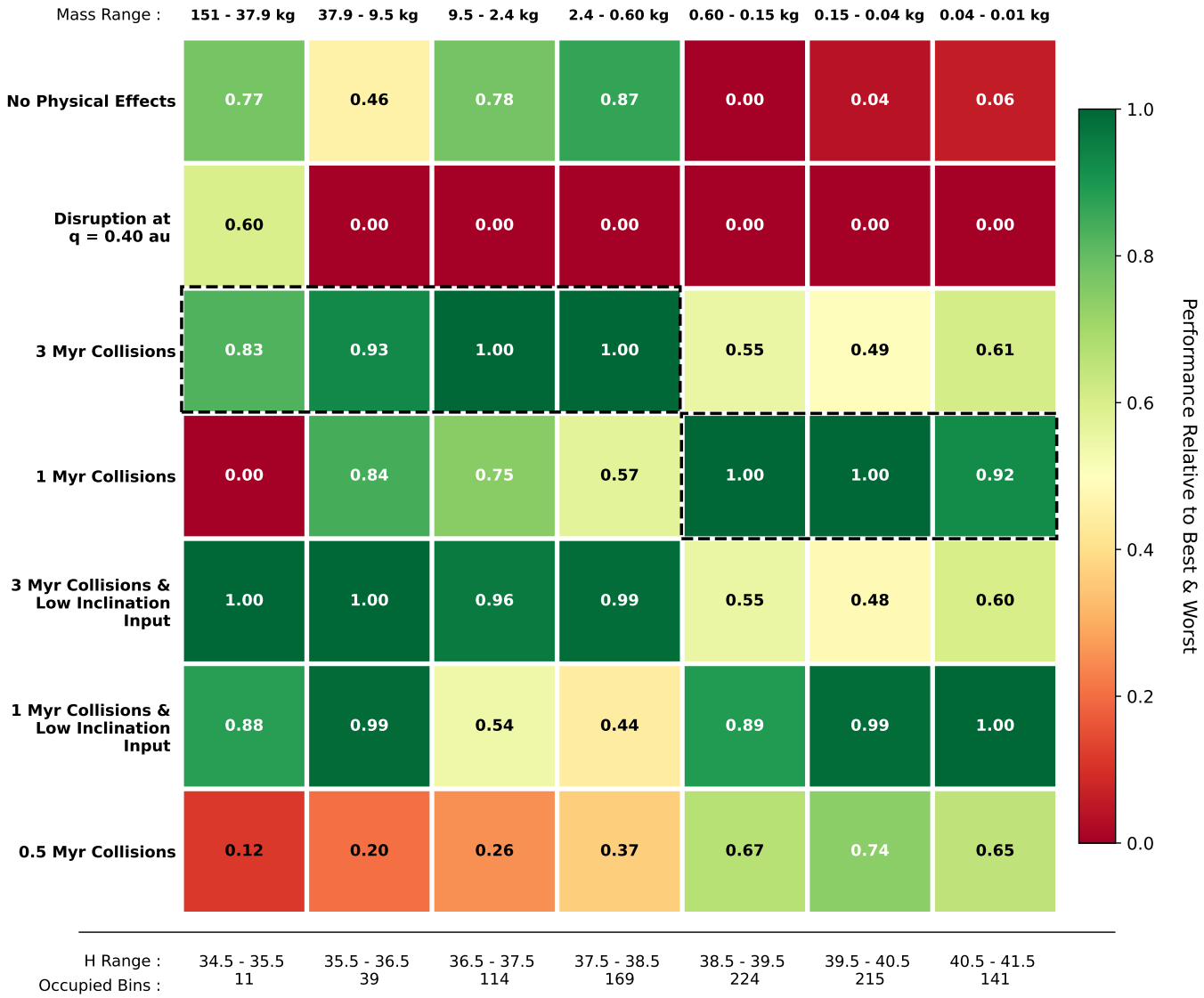

Figure 4. The relative performance of all the models over brackets of decreasing size. Performance is measured by taking the log-likelihood values of the model fit and the data in each size bracket (vertical column) and rescaling them to the range 0–1, between the lowest and highest log-likelihood values. Our choice of best-fit model is shown with the dashed line, switching physical process types at $H = 38.5$ (0.6 kg). The number of bins in $N(a, e, i, H)$ occupied by meteoroids in each size bracket varies, as indicated below each column, and indicates the reliability of the performance measure. The fewer the data, the more sensitive the model is to the presence of individual data points as opposed to general trends. Note this does not add to 1202 as multiple calibration meteoroids can occupy the same bin.

20 difference in efficiency between ν_6 and 5:2J for a collisional lifetime of 3 Myr (A. Morbidelli & B. Gladman 1998). This phenomenon is evident in the change from outer- to inner-belt dominance among kilometer- and subkilometer-sized asteroids in the G18 and NEOMOD models, and it appears to continue regulating the meter population.

5.2. Outer-belt Contribution

Our model predicts a nonnegligible contribution from the 5:2J and 2:1J outer-belt sources, which is not predicted for NEOs of 10 m diameter by previous models. For $H = 25$, G18 requires an outer-belt contribution only from JFCs, and NEOMOD requires only 8:3J; further, NEOMOD2 finds no significant (>2%) outer-belt source contribution for $H = 28$. We propose several explanations for this.

First, though Yarkovsky mobility still explains the overall inner-belt dominance, we see a greater outer-belt signal than comparative models because of a *reduced* mobility of submeter-sized meteoroids relative to their 10 m counterparts, leading to a lower proportion of meteoroids jumping the outer-belt resonances. One-meter meteoroids can exhibit a reduced average Yarkovsky drift over 1 Myr compared to 10 m asteroids, by as much as a factor of 10, because these objects either collide or disrupt on short timescales, interrupting their migration toward the strong ν_6 and 3:1J resonances (W. F. Bottke et al. 2006). The effectiveness of the Yarkovsky force also diminishes when the thermal penetration depth of solar heating exceeds the body's diameter. Such reductions apply only to high-conductivity surfaces, however, i.e., bare rock, whereas for dusty or porous bodies the strength of the Yarkovsky force, and therefore the semimajor axis drift rate, is roughly constant for asteroids of 1 m to 10 m in size.

Second, the YORP effect is another thermal-reradiation interaction that reduces the flux of small asteroids entering escape routes (A. Morbidelli & D. Vokrouhlický 2003; M. Granvik et al. 2017) by altering an asteroid's obliquity

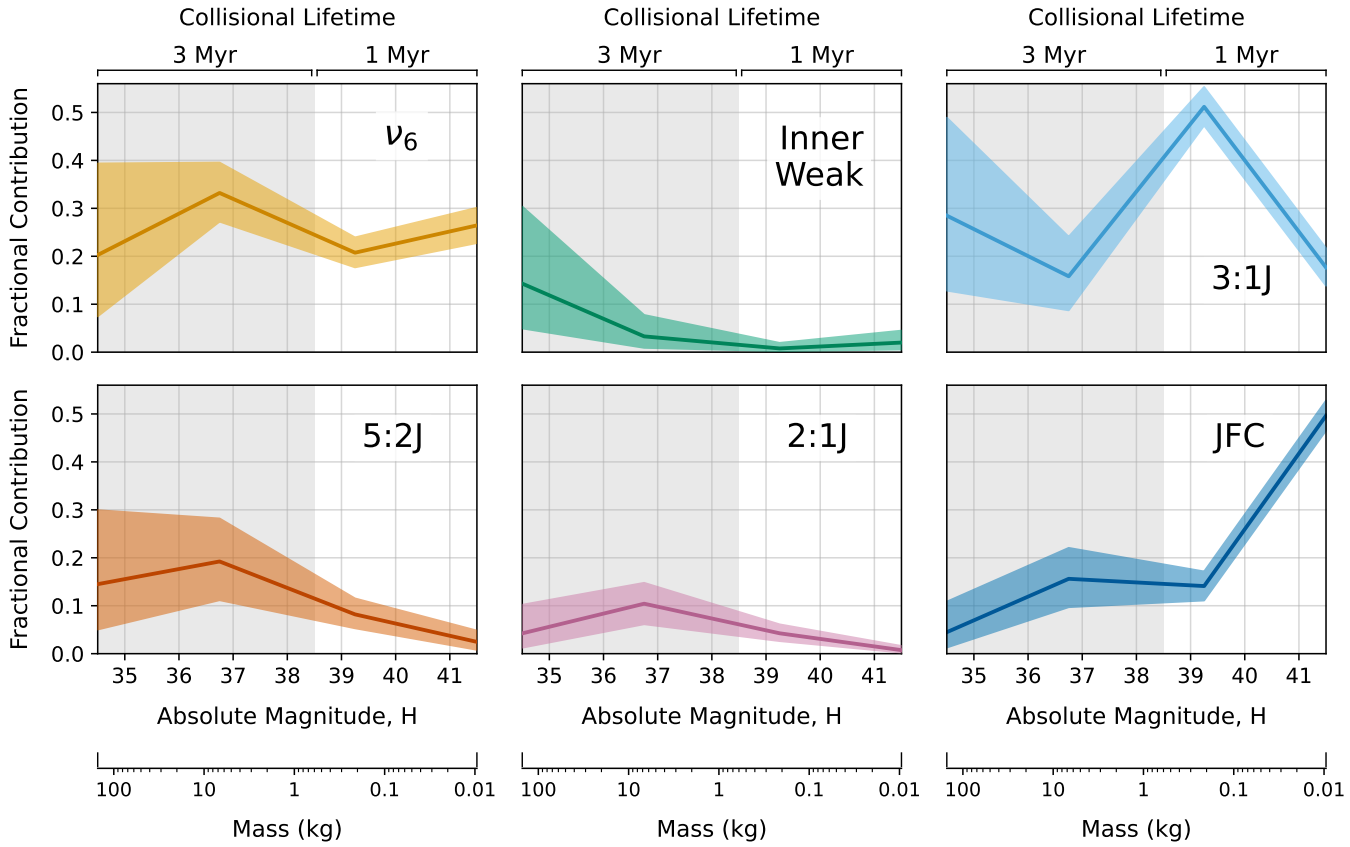

Figure 5. The relative contributions of the six sources, inner weak, ν_6, 3:1J, 5:2J, 2:1J, and JFC, for the optimal three-slope model as per Table 2. There is a transition between input sources with collisions at 3 Myr and 1 Myr lifetimes, as indicated by the gray background.

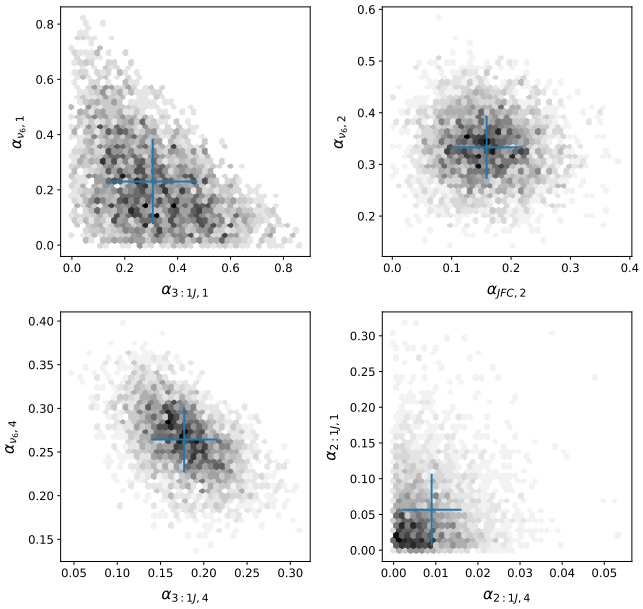

Figure 6. Four examples of posterior distributions from `multinest` for the best-fitting model showing major degeneracy (top left), a well-constrained parameter (top right), minor degeneracy (bottom left), and low-to-zero contribution (bottom right).

and spin rate, interrupting the semimajor axis drift at shortening timescales $\propto$ radius^2. The YORP effect combined with the Yarkovsky force could reduce asteroid drift rates as a function of decreasing size for asteroids $\leqslant$1 m and decrease their ability to jump over weak resonances, thereby reintroducing the contribution from the weaker, outer-belt resonances 5:2J and 2:1J.

A third explanation is a greater quantity of centimeter-to-meter debris near outer-belt resonances, as this region is dominated by hydrated, friable, carbonaceous bodies (F. E. DeMeo & B. Carry 2013, 2014), which are more prone to fracturing during impacts or thermally fragmenting (J. Molaro et al. 2020; M. Delbo et al. 2022; P. M. Shober et al. 2025b).

Our model interestingly predicts a negligible contribution from these sources for much smaller debris ($<$200 g or $\lesssim$5 cm), which we interpret as a relative increase in material coming from other sources (Figure 5) rather than a decrease in outer-belt material. Additional studies on the strength of the Yarkovsky and YORP effects, as well as submeter asteroid strength, would clarify the drivers of the outer-belt signal.

5.3. Increase in Jupiter-family Comet Source Contribution

As we examine the smallest meteoroid sizes in the dataset, we have a much greater contribution from $R_{\rm JFC}$ within our model (Figure 5). The interpretation of the JFC source here, however, must be taken with caution. JFCs are short-period, low-inclination comets largely deriving from the Kuiper Belt and scattered disk as a result of a series of chaotic close encounters with Neptune and Jupiter (J. A. Fernández 1980; H. F. Levison & M. J. Duncan 1994; M. J. Duncan & H. F. Levison 1997; M. Duncan et al. 2004; R. P. Di Sisto et al. 2009; D. Nesvorný et al. 2017). Their orbital evolution is characterized by their close encounters with the gas giant, which cause large chaotic changes in their orbits over

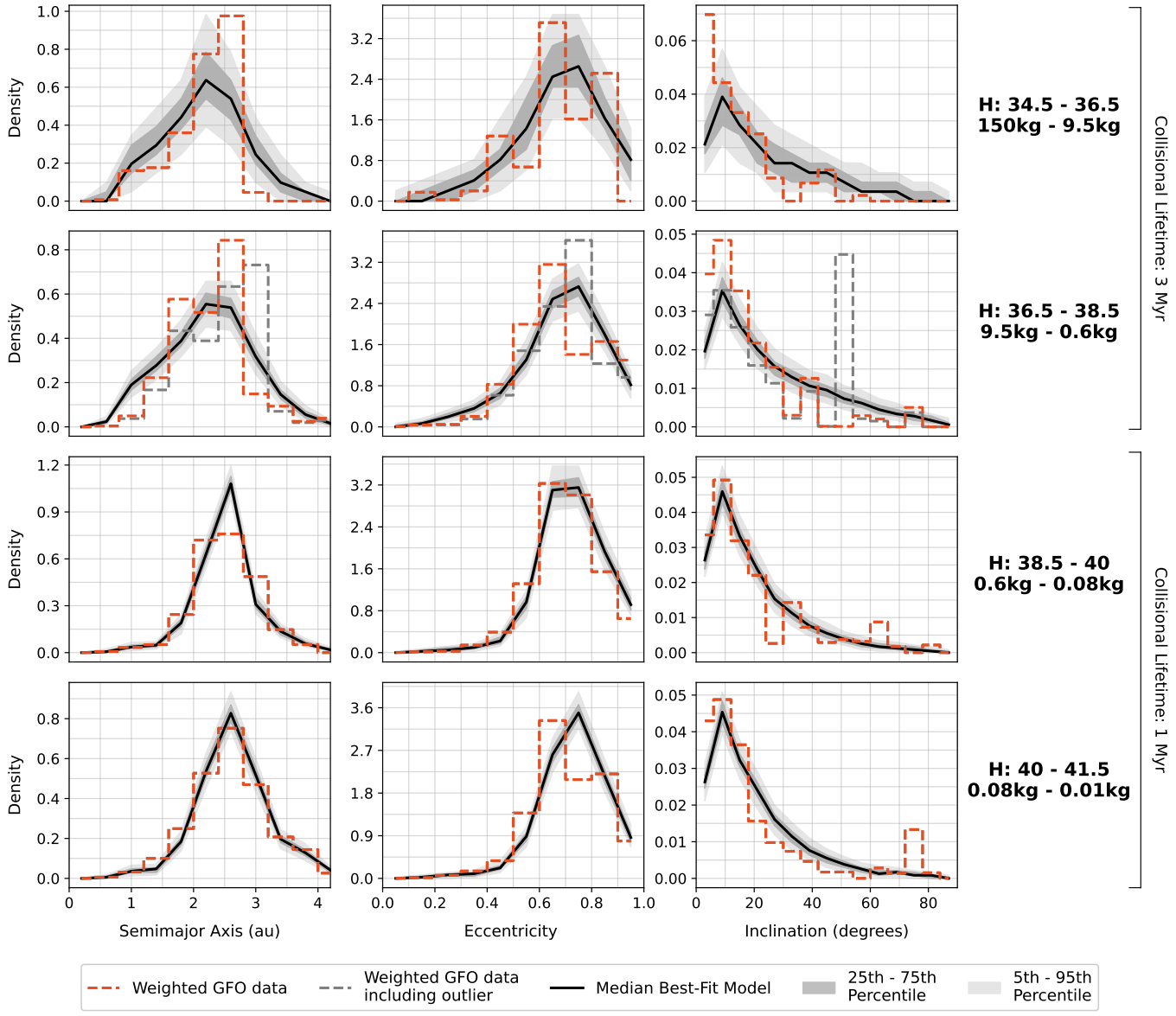

(a)

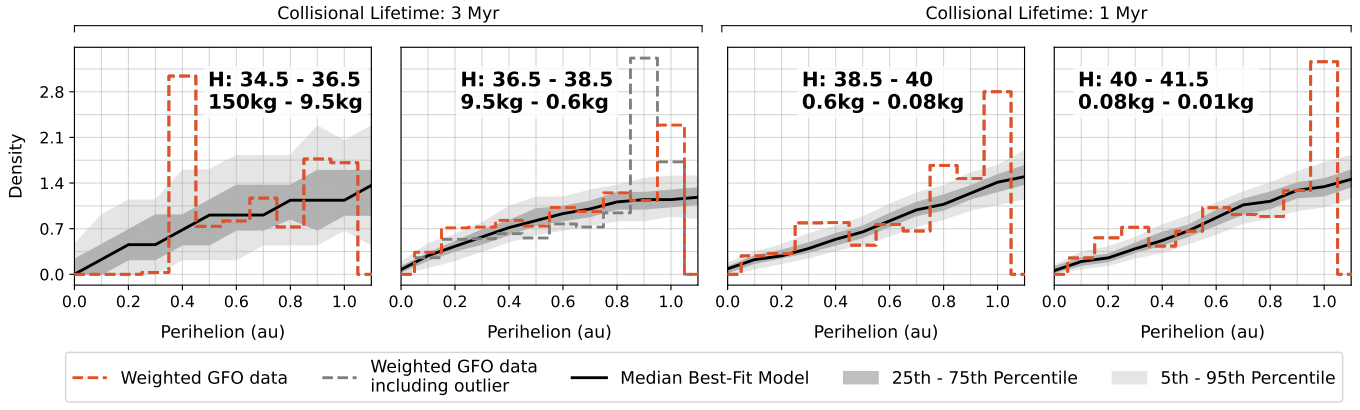

(b)

Figure 7. Normalized orbital-element distributions of the debiased Earth-impacting meteoroids and best-fit model for (a) Earth-crossing orbits ($q < 1.016$ au and $Q > 0.98$ au) and (b) orbits truncated to $q \leqslant 1.1$ au. Two-hundred model outputs were created sampling the parameter uncertainties as described in Section 4.2, and sampled 53, 320, 425, and 425 times for the ranges $H = 34.5$–36.5, 36.5–38.5, 38.5–40, and 40–41.5, respectively. Though sampled as continuous distributions, the histograms here are plotted with 0.4 au, 0.1, 6°, and 0.1 au resolution over the semimajor axis, eccentricity, inclination, and perihelion axes, respectively.

thousand-year timescales (G. Tancredi 1995; H. F. Levison & M. J. Duncan 1997; R. P. Di Sisto et al. 2009; D. Nesvorný et al. 2017). $R_{\rm JFC}$ was created by augmenting the statistics of comets within the model of D. Nesvorný et al. (2017) that reach below $q < 1.3$ au and $a < 4.5$ au (see D. Nesvorný et al. 2023 for a full description of $R_{\rm JFC}$). In this framework, any $R_{\rm JFC}$ contribution at centimeter-to-meter sizes need not indicate a purely cometary (volatile-rich) physical origin, nor a dynamical coupling with Jupiter; it primarily reflects the locations of meteoroids in (a, e, i) space.

Meteoroids on JFC-like orbits are predominantly stable (P. M. Shober et al. 2021, 2024), despite the fact that nongravitational forces (Poynting–Robertson drag, Yarkovsky force, etc.) are not strong enough to decouple these meteoroids from Jupiter. We therefore expect our model to be predicting a source of *stable* JFC meteoroids, for which we present two plausible explanations: (1) centimeter- to meter-sized JFC debris is produced during cometary splitting events of low-q comets that are already dynamically stable, or (2) asteroidal material from an outer-belt source has diffused onto JFC-like orbits.

Since the Earth is located within the inner solar system, the JFC population it samples is not very representative. Only about one-third of JFCs become part of the "visible population" ($q < 2.5$ au), and only one-fifth reach Earth-crossing orbits (H. F. Levison & M. J. Duncan 1997; J. A. Fernández et al. 2002; J. Horner et al. 2004). Despite an average dynamical lifetime of $\sim 1.5 \times 10^5$ yr, JFCs that reach the inner solar system only spend $\sim 10^3$ yr of that time <2.5 au (M. Duncan et al. 1988; H. F. Levison & M. J. Duncan 1994). This limited dynamic lifetime results from both the frequent close encounters with Jupiter and the predicted short physical lifetimes of small JFCs in the inner solar system (10^3–10^4 yr; H. F. Levison & M. J. Duncan 1997; J. A. Fernández et al. 2002; R. P. Di Sisto et al. 2009). Consequently, a JFC that enters into a stable state can break down, split, and produce centimeter- to meter-sized debris (H. Boehnhardt 2004; P. Jenniskens 2008a, 2008b; Y. R. Fernández 2009) along the stable orbit. This hypothesis is potentially supported by the observation that nearly all JFC-like ($2 < T_{\rm J} < 3$) meteor showers (e.g., α-Capricornids, Southern δ-Aquariids, etc.) are more stable than the local sporadic background (Figure 17 within P. M. Shober et al. 2024) and the specific example of the Taurid complex and its primary parent comet 2P/Encke, which is decoupled from Jupiter. The only cometary shower that suffers frequent close encounters with Jupiter is the October Draconids—associated with JFC 21P/Giacobini-Zinner—which is consistent with their observed low-density, fragile meteoroids (J. Borovička et al. 2007; P. M. Shober et al. 2024). Although possible, we consider this explanation unlikely, as JFCs entering onto more stable trajectories decoupled from Jupiter are very rare (J. A. Fernández et al. 2002). H. H. Hsieh & N. Haghighipour (2016) found 0.1%–1% of objects transferred from the JFC region are expected to evolve onto detached orbits, a value 4–40 times lower than the observed rate of stable near-Earth comets (J. A. Fernández & A. Sosa 2015; P. M. Shober et al. 2024). A large supply of centimeter-to-meter cometary debris would also be inconsistent with Zodiacal Cloud (ZC) models, which show that JFCs supply the majority of zodiacal dust through cometary splitting events (D. Nesvorný et al. 2010, 2011; J. K. Rigley & M. C. Wyatt 2022), indicating that the physical lifetimes of this centimeter-to-meter JFC debris must be limited such that it eventually produces <100 μm dust.

This widespread stability among JFC-like cometary showers, together with the unique dynamical and physical properties of the October Draconids, points toward another explanation: asteroidal cross-contamination. The main asteroid belt is a much larger, closer, and more stable source that could be feeding these comet-like orbits with carbonaceous material. Several studies of asteroidal contamination have found that outward diffusion of outer-belt asteroids is capable of explaining the asteroids on cometary orbits (ACOs) that move on stable orbits (J. A. Fernández et al. 2002; J. A. Fernández & A. Sosa 2015; H. H. Hsieh et al. 2020; P. M. Shober et al. 2020, 2024). Infrared catalogs show $\sim$20% of ACOs have asteroid-like low albedos ($p_V > 0.1$; Y. Kim et al. 2014). Further, comet-like spectra dominate only for $T_{\rm J} \lesssim 2.8$; the $2.8 < T_{\rm J} \leqslant 3.1$ interval is a mixed regime with primitive and silicate objects in comparable proportions, with the comet-like fraction increasing toward fainter absolute magnitudes (N. Simion et al. 2021). Based on the arguments above, the main-belt origin seems to be the most likely of these two explanations for the threefold $R_{\rm JFC}$ increase from $H = 39.125$ ($\sim$5 cm) to $H = 41.5$ ($\sim$1 cm). Further work examining the physical breakdown of material from different sources (JFC, carbonaceous, etc.) using thermophysical models is needed to better understand the sources of small centimeter-scale meteoroids.

5.4. Physical Processes

We indirectly observe a collisional lifetime that decreases with size, a trend that could only be identified through the size-dependent analysis used here. We reaffirm the range 1–3 Myr is indeed correct for these sizes, with 3 Myr applying down to objects as small as approximately 0.6 kg (7 cm in diameter, assuming a density of 3500 kg m^{-3}) and transitioning to 1 Myr for smaller objects. This is evident in the relative performance of the collisionally depleted models over various size brackets (Figure 4), as well as the match in slope of the semimajor axis distributions between calibration fireballs and the model output at low ($\leqslant$1 au) values, which visibly changes with decreasing meteoroid size and collisional lifetime (Figure 7). Previous application of main-belt collision models to near-Earth space estimates a collisional half-life of 1–3 Myr for 1 cm–10 cm (D. Nesvorný et al. 2024b), which matches chondritic fireball entry velocities (3 Myr; A. Morbidelli & B. Gladman 1998), though is below the 6 Myr predicted for 10 g meteoroids of both asteroidal and cometary origin (R. H. Soja et al. 2019, their Figure 1). As meteoroid sizes decrease, their physical lifetimes are expected to continue decreasing until reaching a minimum at around 0.1 g (P. Jenniskens et al. 2024). A different implementation of this type of modeling would have to be considered for <10 g. Collisions with the ZC begin to dominate at smaller masses, and these assume a different orbit dependency to main-belt collisions (P. Pokorný et al. 2024). Our estimates and the model fit are global averages of a diverse set of objects, so we do not make strong claims as to the exact meteoroid size of the transition from 3 Myr to 1 Myr. This became clear when the crossover index shifted between models fit to calibration data divided into two groups (see Appendix E). Our model demonstrates NEOs across many

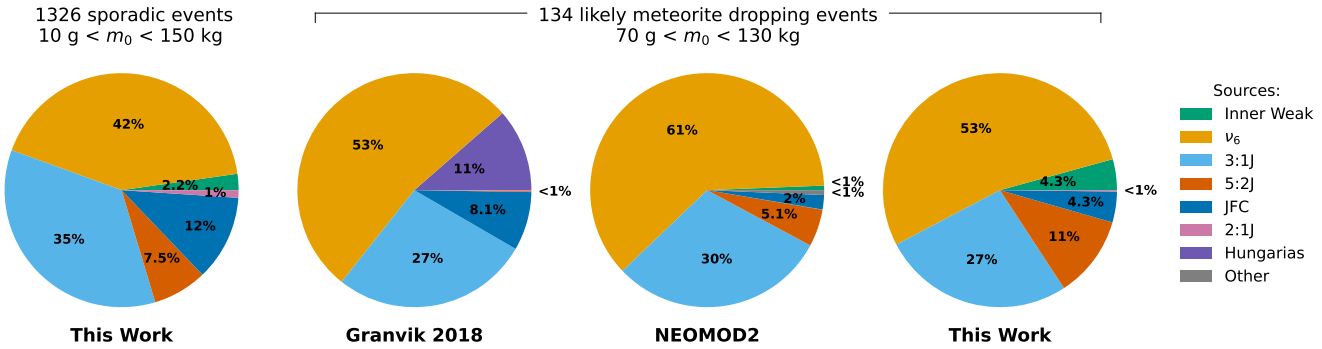

Figure 8. The sources of GFO meteoroids predicted by our nominal, best-fit model, the Granvik 2018 (G18) model, and the NEOMOD2 model. Each event contributes its fractional source probabilities (e.g., 80% ν_6, 10% 3:1J, 10% inner weak), and the chart shows the sum of these fractions, normalized over all events in order to evaluate the population as a whole. The first subgroup contains all sporadic GFO events with initial meteoroid masses $m_0 > 10$ g from 2014 to 2024. The second subgroup restricts to possible meteorite droppers following the likely meteorite-dropper criteria of E. K. Sansom et al. (2019). The lowest initial mass of 70 g for this subset is a consequence of the dropper selection criteria.

sizes are compliant with our current understanding of collisions in the solar system.

Thermal effects are not necessary to describe the orbital distributions of Earth-impacting meteoroids ranging from 1 cm to 0.5 m to the resolution of the data in this study. The low-perihelion disruption model was not preferred over the collisional model (Figure 4), and in some instances performed worse than the base model. It is clear the removal of highly eccentric orbits (Figure 2; the result of removing simulation particles reaching $q \leqslant 0.4$ au) provides a poor fit to the fireball data. It is likely the extrapolation of the critical distance to $q = 0.4$ au following the trend in M. Granvik et al. (2016), which has only been measured for NEOs $\geqslant$50 m, was not appropriate. While telescopic surveys have found meteoroid orbits to be consistent with the $q = 0.4$ au disruption (A. Lue et al. 2019), studies of meteorites and near-Sun dwell times indicate some meteoroids do spend time near the Sun, possibly hinting that the meteorite precursors are fragments of low-q super-catastrophic destruction (A. Toliou et al. 2021). We also conclude that near-Sun approaches do not appear to destroy the meteorite precursors, consistent with the notion that meteoroids are often monolithic (J. Borovička 2016; T. Kareta et al. 2024) and withstand greater thermal stresses than rubble-pile asteroids. New thermal effects would need to be considered for objects smaller than those modeled here, as it has been observed that lifetimes of primarily comet-derived material $\leqslant$1 cm have a q dependency (P. Jenniskens et al. 2024). Further modeling of the combination of collisional and thermal processes on the centimeter- to meter-sized NEO population is required to determine the extent to which these phenomena affect the smallest NEOs and connect to the depletion and creation of asteroids, meteoroids, sporadic cometary material, and dust particles.

5.5. Lack of Hungarias

The Hungaria region ($a \sim 1.8$ au, $i \sim 15°$–$20°$) is a significant source of large NEOs in the G18 model ($\sim$20% for $H = 25$), and to a lesser extent in NEOMOD2 ($<$2.9% for $H = 28$). The proportion of NEOs originating from the Hungaria region in the G18 model varies considerably with asteroid size, but tends to be magnified by their long dynamical lifetimes, particularly at both the large ($H = 17$, $\sim$12%) and small ($H = 24$, $\sim$20%) ends of the populations. The Hungaria group are made up mainly of Xe-type, S-type, and some C-type asteroids (M. P. Lucas et al. 2017). The largest of the group—434 Hungaria—is an Xe type (S. J. Bus & R. P. Binzel 2002), and also is the leading member of a collisional family (J. G. Williams 1992; A. Lemaitre 1994).

Based on G18 and NEOMOD2, one would expect Xe-type material to represent a prominent source of meteorites on Earth. It has been proposed that Xe-type asteroids are associated with enstatite achondrites (aka aubrites), based on both albedo and spectrum indications (M. J. Gaffey et al. 1992) and dynamics matching meteorite ages (M. Ćuk et al. 2014). However, these enstatite achondrites only represent $\sim$1% of meteorite falls (see the *Meteoritical Bulletin*[28]), so there is a mismatch. Our model confirms this mismatch: the Hungaria source region is not a preferred contributor of Earth-impacting NEOs in our size range (see Section 4.1).

The Xe-type Hungaria collisional family is a relatively old asteroid family (207 $\pm$ 65 Myr old; F. Spoto et al. 2015). As the Yarkovsky drift rates are high at meteoroid sizes $\pm$[0.01–0.001] au Myr^{-1}, these objects can reach nearby resonances as early as a few million years after the collision, rapidly depleting the region of small debris and feeding near-Earth space. Following the Hungaria family-forming event, it is probable that small Xe-type impactors could have been a major source of meteorites then. However, this increase would have dissipated a long time ago, within tens to a hundred million years of the family-forming event. We still occasionally get small Xe-type meteorites landing on Earth, but these are likely the result of more recent collisions. Interestingly, asteroid 2024 BX1, which delivered the Ribbeck enstatite achondrite (A. Bischoff et al. 2024), has a negligible chance of having come from the Hungaria source region when using NEOMOD (ν_6, 88.1%; 3:1J, 10.9%; 5:2J, 0.2%; inner weak, 0.7%; Hungarias, 0.1%). Assuming the Xe type = enstatite achondrite connection holds, this could mean enstatite achondrites have another source in the belt, distinct from the Hungaria collisional family.

5.6. Earth-impacting Population Predictions

For each GFO event's orbital elements (a, e, i, H), we calculated the fractional contribution to those coordinates from each of the sources as predicted by our model using the median α_s values reported in Table 2 and the original R_s binning. We show the sum of the fractional probabilities for all events (as

[28] www.lpi.usra.edu/meteor

opposed to counting the maximum probability per event) to have a population-wide overview of source probabilities in Figure 8. The sources that predominantly feed the Earth-impacting population are the ν_6 and 3:1J resonances, contributing to 74% of the sporadic GFO fireballs caused by meteoroid >10 g. When we restrict our sample to likely meteorite-dropping events, described in Appendix F, we expect 83% of the meteoroids to originate from the inner main belt (ν_6, 53%; 3:1J, 26%; inner weak, 4%). This is slightly less than NEOMOD's 91% prediction for simulated Earth impactors (ν_6, 57.6%; 3:1J, 29.7%; inner weak, 3.8%—as calculated from their $\alpha_j(H = 25)$ and $f_{\rm imp}$ parameters) and on par with the 88% prediction for meter-scale Earth impactors from P. Brown et al. (2016) using the W. F. Bottke et al. (2002a) model (intermediate source Mars crossing, 26%; ν_6, 48%; 3:1J, 14%). Feeding our likely meteorite-dropping GFO events into the NEOMOD2 model with a preset size $H = 28$ yields predictions similar to those of our model (Figure 8). Both models have twice as many bodies arriving from the ν_6 resonance compared to the 3:1J resonance. Our model predicts a greater chance of arriving from each of the remaining sources—inner weak, 5:2J, and JFC—by about a factor of 2. P. Brown et al. (2016), using W. F. Bottke et al. (2002a), predict 8% outer-belt and 4% JFC contributions to meter-scale impactors, where 10/55 analyzed events are also confirmed meteorite droppers. All models allocate a negligible chance of the likely droppers arriving from the 2:1J resonance, or any other minor sources. These predictions are not necessarily an indication of the amount of pristine material that is reaching us, however. These NEO models do not provide any information about the type of material arriving from each source (besides from NEOMOD3, which includes asteroid albedo). As a result, when using them to predict which source meteorite droppers come from, we are assuming that material from all sources has an equal probability of surviving atmospheric entry. In reality, this is not the case: If a likely meteorite dropper has an equal chance of *dynamically* arriving from an inner- and outer-belt source, it is more likely to be from the inner belt, which is the primary source of generally stronger ordinary chondrite meteorites, whereas the outer-belt is the main source of weaker carbonaceous chondrites (R. P. Binzel et al. 2019; M. Brož et al. 2024a, 2024b; P. Jenniskens & H. A. R. Devillepoix 2025). Until we can quantify survivability as a function of source region, we must acknowledge these probabilities are biased.

When we compare the maximum source probability for each event, our model's results are nearly identical to the NEOMOD2 predictions for the GFO likely meteorite droppers. This is somewhat expected considering we are using the R_s distributions derived from the same numerical simulations, and the source strengths for our dominant sources at $H = 28$ and $H = 34.5$ are nearly the same. Even though collisions were included in our model, it was implemented in the same way for all sources, so they would not significantly change the source ratios per orbital bin in comparison to a collisionless model. This speaks to the strength of the extrapolation of the NEOMOD models and its application to the near-Earth meteoroid environment.

5.7. Link to Asteroid Families

The attempts to connect meteorite types to asteroid families is a complex task, one informed through asteroid observation, classification (F. E. DeMeo et al. 2022) and association with meteorite analogs (A. Battle et al. 2025; A. McGraw et al. 2025), modeling of NEO delivery (M. Brož et al. 2024a, 2024b; M. Marsset et al. 2024), and observing meteorite preimpact orbits to associate them with specific escape routes (P. Jenniskens & H. A. R. Devillepoix 2025) or with known NEOs (J. Borovička et al. 2015; P. M. Shober 2025; P. M. Shober et al. 2025a).

From the study of asteroid family ages and expected size–frequency distributions, M. Brož et al. (2024a) model the relative contribution of the Phocaea family to NEOs as decreasing with size, from 8.7% for 1 km-sized NEOs to a negligible contribution (0.7%) for 1 m-sized impacting meteoroids. We also see no significant contribution from Phocaea in our model for near-Earth meteoroids (<1 m). P. Jenniskens & H. A. R. Devillepoix (2025) also do not think Phocaeas supply many H-type chondrites—the meteorite type associated with the family—from the lack of orbital meteorites seen to originate from highly inclined inner-belt orbits still found in the 3:1 resonance. The residing orbits of small H-type candidate (<300 m) NEOs are also dynamically consistent with a ν_6 or 3:1J origin, with none observed thus far connected to the Phocaeas (J. A. Sanchez et al. 2024).

Additionally, there is a debate as to whether L-type chondrites come from the Massalia family (M. Marsset et al. 2024) or the Nysa/Hertha family (P. Jenniskens & H. A. R. Devillepoix 2025). Both are young asteroid families at low inclinations ($1\overset{\circ}{.}4$ and $2\overset{\circ}{.}4$) between the ν_6 and 3:1J resonances. High-resolution simulations of these families evolving onto Earth-crossing orbits may reveal distinctive orbital distributions. By comparing the resulting near-Earth orbital distributions with observations—as demonstrated here by our low-inclination tests—it may become possible to identify which family is the dominant contributor of L-type chondrites, i.e., alike to METEOMOD.[29]

5.8. Implications for the Decameter NEOs

Work to investigate the population of decameter NEOs (∼10 m diameter) is most difficult due to the lack of observations in this size range (I. Chow & P. G. Brown 2025); however, we can make several inferences using our model. (1) The inner main belt, which predominantly supplies NEOs >10 m in diameter (W. F. Bottke et al. 2002a; M. Granvik et al. 2018; D. Nesvorný et al. 2023) and NEO meteoroids <1 m (this work), is the primary source of the decameter NEO population. (2) The low-perihelion disruption process, as currently implemented in M. Granvik et al. (2018) and D. Nesvorný et al. (2023) and extrapolated from M. Granvik et al. (2016), ceases to apply for NEOs ⩽10 m. Such a change could alter the orbital distribution and size–frequency distribution of decameter NEOs in ways that are yet understood. Recent investigation into the perihelion history of NEOs shows that meteorite precursors likely dwell at low perihelion distances (A. Toliou et al. 2021), and that low perihelia preferentially remove weaker material from the Earth-impacting <1 m population (P. M. Shober et al. 2025b). Since previous studies have already demonstrated the role of solar processing in NEO evolution, continued investigation of size-dependent thermal alteration processes is particularly

[29] https://sirrah.troja.mff.cuni.cz/ mira/meteomod/meteomod.html

important for understanding the hazardous Earth-impacting population.

6. Model Limitations

We highlight several limitations of this model for future users. First, the model is calibrated only to meteoroids in the Aten and Apollo dynamical classes, as Atira and Amor objects do not cross Earth's orbit. Second, the JFC source region is adopted from NEOMOD without modification. This does not account for cometary fragmentation or dispersion of centimeter-sized particles. Improved input distributions bridging between those for millimeter-sized particles (D. Nesvorný et al. 2010, 2011) and those for comets (D. Nesvorný et al. 2017) would help confirm our interpretation of the JFC contribution. Third, the model is fit in $\log(m)$ rather than absolute magnitude H. We used a single conversion to H based on ordinary chondrites/S-complex asteroids. Fitting a model using informed physical properties per meteoroid, such as using fireballs with measured spectroscopy (V. Vojáček et al. 2015), would be more accurate when translating the results into H. Finally, the model uses meteoroids biased in size, as we do not yet have a method to debias the GFO data in terms of absolute numbers. Model interpretation must therefore be performed over discrete size brackets, as done here (Figure 7), and meteoroid orbit generation must likewise be carried out in discrete size bins, unless the user imposes their own size–frequency distribution for the flux of Earth impactors.

7. Model Application

We promote the use of this model to investigate NEOs in the 1 cm to 1 m size range. We provide the resources to (a) query the source-region probability of orbits and (b) generate meteoroid orbital distributions on Zenodo (doi:10.5281/zenodo.17809512; S. E. Deam & D. Nesvorny 2025). We suggest that previous calculations of the origin of meteoroids using NEOMOD do not need to be repeated, as the fractional contributions of sources are the same for the most dominant sources (Section 5.6). However, we do note a difference between predictions by this model/NEOMOD and predictions by the G18 model, such as in M. Granvik & P. Brown (2018) or I. Chow & P. G. Brown (2025). The main strength of sampling orbits from this model lies in the difference in orbital-element distributions between the model (1 cm–1 m) and all other NEO models (>10 m), due to the inclusion of size-dependent collisions, removing highly evolved orbits.

8. Conclusion

This work utilized the unique dataset of 1202 sporadic meteoroids of mass >10 g observed by the GFO to create a debiased model for NEOs. This model covers meteoroids from 10 g to 150 kg in size (approximately 1 cm to 0.5 m in diameter) dynamically evolving from the main asteroid belt onto Earth-crossing orbits, experiencing collisions while still coupled to the main belt, which depletes the population of highly evolved orbits, e.g., low-semimajor-axis and high-inclination orbits. The major findings of this model are as follows:

1. We observe a global decrease in collisional half-life from 3 Myr to 1 Myr for the meteoroid population, with a transition at around 0.6 kg/7 cm. This aligns with current understanding and estimates of collision processes.
2. The model shows an increase in JFC-type orbits contributing to near-Earth meteoroids for sizes smaller than 5 cm (250 g).

This model, along with previous NEO models, borders the decameter size range—a population that is difficult to observe and potentially hazardous to civilians from airbursts in the atmosphere. The inferences we can make about the decameter population are as follows:

1. The inner main belt (ν_6 secular resonance, 3:1J and various weak mean-motion resonances 2.1–2.5 au) continues to dominate feeding the near-Earth meteoroid population across 10 m to 1 m diameter objects.
2. There is a change in the near-Sun disruption trends for asteroids smaller than 10 m, as M. Granvik et al.'s (2016) low-perihelion disruption law extrapolated to 0.4 au does not directly apply to 1 m diameter meteoroids.

Overall, we find strong motivation to continue investigating and modeling decimeter meteoroids, particularly on the physical processing of these bodies near the Sun or the low-inclination delivery into resonances by young asteroid families. We therefore encourage the community to continue observing fireballs in the night sky.

Acknowledgments

The Desert Fireball Network and Global Fireball Observatory programs have been funded by the Australian Research Council as part of the Australian Discovery Project scheme (grant Nos. DP170102529, DP200102073, and DP230100301), the Linkage Infrastructure, Equipment and Facilities scheme (grant No. LE170100106), and received institutional support from Curtin University. S.E.D. acknowledges the support of an Australian Government Research Training Program Scholarship. L.D. thanks the STFC (grant Nos. ST/Y004817/1, ST/T002328/1, ST/W001128/1, and ST/V000799/1) for support. C.D.K.H. acknowledges the support of the Canadian Space Agency FAST grant Nos. 18FAALBB20 and 21FAALBB17, and Natural Sciences and Engineering Research Council of Canada grant No. RGPIN-2018-04902. P.B. was supported by NASA cooperative agreement 80NSSC24M0060.

Software: Rebound (H. Rein & S. F. Liu 2012), PyMultiNest (J. Buchner et al. 2014), Matplotlib (J. D. Hunter 2007), NumPy (C. R. Harris et al. 2020), pandas (The pandas development team 2025), SciPy (P. Virtanen et al. 2020).

Appendix A
Data: Quality Cuts and Fireball Selection

Capture geometry. Meteoroids were only included in the model calibration if the best convergence angle of the data captured was above 10°. The convergence angle describes the angle between the image planes of two camera observations. As a single image can only localize a fireball within the two-dimensional image plane, the observation of a second camera provides a constraint on the distance to the fireball in the dimension perpendicular to the first image plane. This has the highest precision when the two image planes are perpendicular: a convergence angle of 90°. Alternatively, if the convergence angle is low, then the two image uncertainties

Table 3
The DN Cutoff Values for Fractional Recovery of Stream Members from D. P. Galligan (2001) Used to Associate GFO Events with Known Meteor Showers

D_N Cutoff		Inclination
90%	70%	(deg)
0.11	0.08	$i < 10$
0.14	0.09	$10 \leqslant i < 90$
0.26	0.17	$i \geqslant 90$

compound and the triangulation is less precise. The location of a meteoroid's entry over a local group of cameras is random, so the convergence angles are not correlated with any particular meteoroid orbit type. Cameras within the GFO network in Australia are typically spaced 100–150 km apart for optimal sky coverage and triangulation. As a result, a minority (∼8%) of the detections have a convergence angle $<10^\circ$ and are disregarded here.

Initial mass. Only meteoroids with a preatmospheric mass of at least 10 g were included in this analysis. This is to ensure we are working with meteoroids with a sufficient mass to be reliably detected by the GFO cameras, which have a limiting magnitude of ∼0.5 (R. M. Howie et al. 2017a). The lower limit of each meteoroid's mass was determined from the dynamics of the luminous flight of the fireball (E. K. Sansom et al. 2015). For the small number (<20) of low-deceleration, nonconverging events, the mass was instead estimated using photometry by integrating the ablation equations of Z. Ceplecha et al. (1998) for the GFO cameras' green-channel light curves using the luminous efficiency of D. O. Revelle & Z. Ceplecha (2001), as done for the European Fireball Network in J. Borovička et al. (2022).

Meteor-shower association. As our intention is to model the sporadic meteoroid population, fireballs created from meteor-shower material were not included when calibrating the model. To identify meteor-stream events in the GFO dataset, an orbit-similarity criterion was computed between all GFO events and the established showers or single-shower entries (status flags 1 and 2 in the database) of the IAU Meteor Data Centre (M. Hajduková et al. 2023).[30] An orbit-similarity criterion is a metric of orbit similarity, first described by R. B. Southworth & G. S. Hawkins (1963), and used to associate meteors together as showers or link them to parent bodies. Here we used the D_N criterion (G. B. Valsecchi et al. 1999) as it is the most appropriate for our on-sky, geocentric measurements (A. V. Moorhead 2016). We associated any GFO fireball with a stream if D_N was below the cutoff retrieval percentages of D. P. Galligan (2001), which we show in Table 3. The more accommodating 90% retrieval cutoff was chosen for 14 major showers (Perseids, Geminids, Orionids, Northern Taurids, Southern Taurids, Northern δ-Aquariids, Southern δ-Aquariids, Quadrantids, α-Capricornids, Leonids, σ-Hydrids, η-Aquariids, Comae Berenicids, and November Orionids) as we were expecting to have many fireball events from these showers in our dataset that we wished to identify and remove, while the more constrained 70% retrieval was used for all other showers.

[30] Downloaded from https://www.iaumeteordatacenter.org/ (Accessed: 2023 August 23).

Appendix B
Data: Correcting for Observational Biases

Detection efficiency. First, we address the in-atmospheric detection bias. Several factors influence the likelihood of a meteor or fireball being detected, including the signal's strength, duration, and the event's location in the sky as viewed by the detector. Several works have independently addressed these biases for both radar and photometric systems, presenting bias-corrected meteor populations (D. P. Galligan & W. J. Baggaley 2005; M. D. Campbell-Brown 2008; P. Jenniskens et al. 2016). Here we aim to correct for our instrument limiting magnitude, which manifests as a bias against detecting smaller, slower meteoroids. The light from a fireball is created by the conversion of kinetic energy to luminous energy, described analytically in Z. Ceplecha et al. (1998). As we do not know the meteoroid's composition, shape, or cross-sectional area, etc., we combined their Equations (1), (2), and (28) to isolate the dependence of luminosity on mass and velocity:

$$I \propto v^5 m^{2/3}, \tag{B1}$$

where I represents the relative luminosity of a fireball, v is the initial velocity of a meteoroid in kilometers per second, and m is the initial mass of a meteoroid in kilograms. We expect every fireball above some brightness to be detected by the GFO cameras and pipeline, while fireballs dimmer than this to have a lower probability of being detected. We assume that such probability scales linearly with the decrease in luminosity. We therefore weight each event by a detection efficiency factor ϵ (Equation (B2)) if the luminosity I falls below some threshold κ, while fireballs brighter than κ have no weighting applied, i.e., ϵ is 1:

$$\epsilon(m, v) = \begin{cases} \frac{I}{\kappa} & \text{if } I < \kappa, \\ 1 & \text{if } I \geqslant \kappa. \end{cases} \tag{B2}$$

The absolute value of the weighting is not important here, only the relative values between fireballs. κ was determined by comparing the entry velocities of the smallest GFO fireballs ($10\,\mathrm{g} < m_0 < 30\,\mathrm{g}$), weighted by the detection efficiency ϵ of Equation (B2), against all-data mass-weighted (up to 30 g) Cameras for Allsky Meteor Surveillance (CAMS) meteors (P. Jenniskens et al. 2016). The match between the distributions, particularly for velocities $>30\ \mathrm{km\,s^{-1}}$, is best with $\kappa = 9.5 \times 10^4$ (Figure 9). The resulting $\epsilon(m, v)$ weighting, plotted in Figure 10, shows that 1073 (89%) of the GFO meteoroids used in the model calibration are above the κ threshold and therefore have $\epsilon = 1$ (i.e., no weighting), and the remaining 129 events (11%) are weighted by $1/\epsilon$.

Earth-impact probability. The following section describes the efforts to debias the GFO meteoroids from the limitation of only observing objects that collide with the Earth, and not uniformly sampling the inner solar system. We account for the meteoroid's probability of impacting Earth and the gravitational focusing of the Earth. After comparing several probability calculation techniques, we decided to use the semi-analytical method of O. Fuentes-Muñoz et al. (2023) to calculate the relative Earth-impact probabilities for each GFO meteoroid. This method is preferred because (a) we know the osculating orbital elements with uncertainties for each meteoroid before impact, including a mean anomaly, (b) the

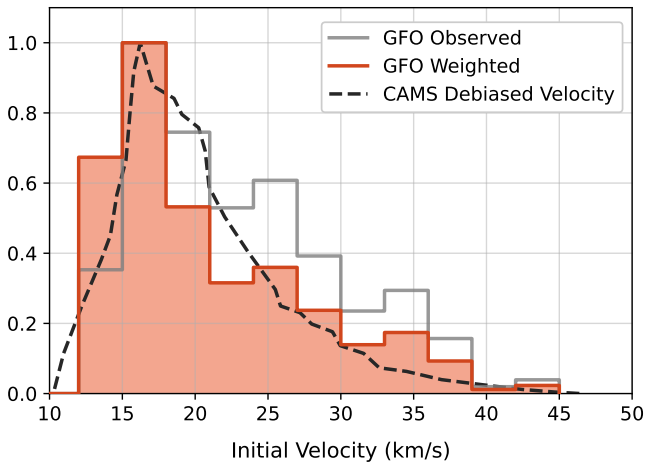

Figure 9. The top-of-the-atmosphere velocity distributions for anti-helion, sporadic meteors from GFO and Cameras for Allsky Meteor Surveillance (CAMS; P. Jenniskens et al. 2016, digitized from their Figure 16) for initial masses of <30 g, normalized by their maximum value. The $1/\epsilon$ weighting from Equation (B2) with $\kappa = 9.5 \times 10^4$ was applied to the GFO events to best reproduce the CAMS distribution.

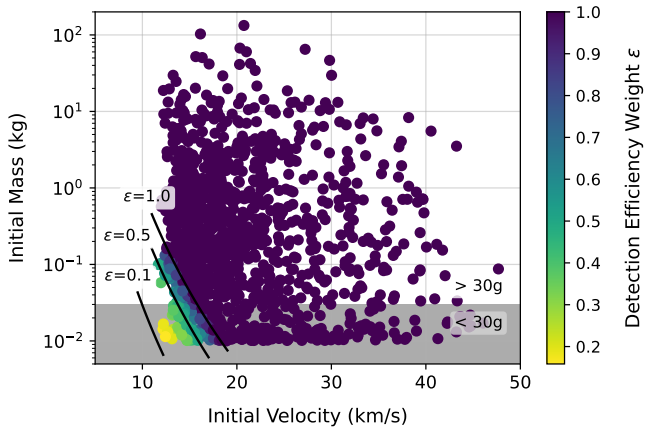

Figure 10. The velocity–mass-dependent detection efficiency weighting. The 1202 calibration meteoroids are colored by ϵ (Equation (B2)). Solid black lines show lines of constant weight. The majority (89%) of events have a weighting of 1. The efficiency decreases with both mass and velocity, indicating that the smallest and slowest events will receive the greatest weighting. The gray background shows the <30 g mass fireballs that were used in the Figure 9 comparison with CAMS data to determine κ.

dynamical lifetimes of NEOs are less than the long-term dynamics perturbations implemented in other impact probability calculations (e.g., D. Vokrouhlický et al. 2012; P. Pokorný & D. Vokrouhlický 2013), and (c) the numerical integrations of this method reduce the assumptions about the previous orbital propagation per meteoroid.

Orbital histories of GFO meteoroids were numerically integrated to evaluate their previous proximity to the Earth and calculate relative Earth-impact probabilities. For each of the 1202 events, a cluster of 200 particles was injected into a `REBOUND` simulation populated with the Sun and the planets from Mercury to Neptune as well as Earth's Moon (H. Rein & S. F. Liu 2012). Each meteoroid's latitude, longitude, altitude, and velocity vector (as measured in the Earth-centered, Earth-fixed coordinate frame) from the highest point of the triangulated fireball were used as initial conditions for the simulated particle. The velocities for the 200 particles were sampled within the fireball measurement uncertainties. With appropriate coordinate transforms, the simulation was populated with these 200 particles and integrated backwards for 100,000 yr using the IAS15 integrator (H. Rein & D. S. Spiegel 2015), while recording the particles' orbits every 10 Earth years.

The Earth-impact probability of each particle was calculated from Equations (1) and (4) of O. Fuentes-Muñoz et al. (2023; Equations (B3) and (B4) below). Equation (B3) here calculates the probability, $P_{\rm MA}$, of the mean anomaly of the Earth and the simulated particle aligning such that there is a close encounter, from the relative velocity between the Earth and particle, U, the orbital periods of the Earth and particle, $T_\oplus$ and T_p, the velocity vectors of the Earth and particle, $\boldsymbol{v}_\oplus$ and $\boldsymbol{v}_p$, and the minimum orbital intersect distance (MOID) between the particle and Earth. The MOID was calculated for each recorded orbital configuration using the algorithm of T. Wiśniowski & H. Rickman (2013).[31] $P_{\rm MA}$ was then calculated for intervals when the MOID was below $d = 0.01$ au, approximately Earth's Hill radius. The impact probability of a particle over the entire integration period T was then calculated as P in Equation (B4), where $K_\oplus$ and K_p are the orbital parameters of the Earth and particle, respectively, at time t. The average probability of the 200 particles was used as the impact probability for the fireball event. The final P was relatively insensitive to both the $P_{\rm MA}$ sampling interval (both 0.25 and 10 yr were tested) and the simulation integration length (most particles per event converge toward the final P within $T = 30{,}000$ yr). For a single GFO meteoroid, we report the relative Earth-impact probability as the median P value of the 200 simulated particles with a nonzero probability. Within a simulation, stochastic processes could result in the ejection of particles from the inner solar system, resulting in some particles with $P = 0$:

$$P_{\rm MA} = \frac{2Ud}{T_\oplus T_p |\boldsymbol{v}_\oplus \times \boldsymbol{v}_p|} \sqrt{1 - \frac{\rm MOID^2}{d^2}}, \tag{B3}$$

$$P = \frac{1}{T} \int_T P_{\rm MA}(d, K_\oplus, K_p) dt. \tag{B4}$$

For meteoroids that approach the Earth's Hill sphere, the effective collisional radius of the Earth depends on the meteoroid's relative velocity because of the mutual gravity between the two objects. Objects with higher relative velocities have smaller effective collisional radii, and therefore a lower chance of impact (E. J. Öpik 1951). We account for such relative gravitational focusing by including an additional weighting to each GFO meteoroid through Equation (B5), where V_∞ is the velocity of the projectile as it first enters Earth's gravitational influence:

$$\left(1 + \frac{1}{V_\infty^2}\right). \tag{B5}$$

Appendix C
Methods: Model Parameters and Optimization

To create a model of the observed meteoroid population, each source region is multiplied by a strength factor, $\alpha_s(H)$, to scale the relative contributions of each meteoroid source. This implements the size-dependent contribution of a source to the

[31] Accessed from https://github.com/mkretlow/MOID.jl.

NEO population, as previously established in the G18 and NEOMOD models. We model this size dependence with m continuous, piecewise linear functions. For m linear functions (or slopes), there are $m + 1$ free parameters. For example, $m = 1$ is a single slope between $H = 34.5$ and 41.5 described by two parameters α_1 and α_2, while $m = 2$ contains three α parameters with an apex at $H_2 = 38$. We varied the number of slopes to best fit the calibration dataset. The strength function for source s is therefore a collection of piecewise functions outlined in Equation (C1), where H_1 and H_{m+1} are the bounds of the H-axis:

$$\alpha_s(H) = \begin{cases} \alpha_{s,1} + (\alpha_{s,2} - \alpha_{s,1})(H - H_1) & \text{for} H_1 < H \leqslant H_2, \\ \alpha_{s,2} + (\alpha_{s,3} - \alpha_{s,2})(H - H_2) & \text{for} H_2 < H \leqslant H_3, \\ \vdots & \vdots \\ \alpha_{s,m-1} + (\alpha_{s,m} - \alpha_{s,m-1})(H - H_{m-1}) & \text{for} H_{m-1} < H \leqslant H_m, \\ \alpha_{s,m} + (\alpha_{s,m+1} - \alpha_{s,m})(H - H_m) & \text{for} H_m < H \leqslant H_{m+1}. \end{cases} \tag{C1}$$

The contributions from the n sources are added together under the constraint that the sum of the strength function for any size H equals 1:

$$\sum_{s=1}^{n} \alpha_s(H) = 1. \tag{C2}$$

The introduction of physical processes, e.g., collisional lifetimes, provided the opportunity to include multiple process types, t, within a single model. This allowed for more freedom, for example, to adjust the collisional lifetime as a function of size. The residence time distribution for source s and process type t, $R_{s,t}$, was selected as a function of size, H, with a simple crossover at size δ. Note that it is possible for δ to equal the boundaries of the H-axis, 34.5 or 41.5, which simply allocates a single type of process over the entire size range:

$$t(H;\, \delta) = \begin{cases} t_1 & \text{for} H < \delta, \\ t_2 & \text{for} H \geqslant \delta. \end{cases} \tag{C3}$$

To summarize, the model fits for the strength factors $\alpha_{s,m+1}$ for n number of main-belt sources s and a chosen number of slopes m, with the crossover between process type t_1 and t_2 at index δ. These parameters combine with the residence time distributions to make the model distribution $N(a, e, i, H)$ (Equation (C4)), where $\alpha_s(H)$ is defined in Equation (C1) and $t(H;\delta)$ is defined in Equation (C3). To be explicit, this model does not fit for the absolute flux of meteoroids in either near-Earth space or as Earth impactors. The flux of the weighted GFO meteoroids was renormalized to the number of meteoroids it represented, i.e., $\int_a\int_e\int_i\int_H N_{\rm GFO}(a, e, i, H) = 1202$, while $\int_a\int_e\int_i\int_H N(a, e, i, H) = 28$ (the R_s sum to 1 for each of he 28 H bins). We chose this because (1) scaling both N and $N_{\rm GFO}$ to match some size–frequency distribution $N(H)$ would not provide any new information, and (2) we do not yet have a method to debias our GFO data in absolute terms (see also Appendix B). We are therefore cautious only to investigate the model output over discrete size brackets in our interpretation and discussion, since the size–frequency of the GFO meteoroids does not match that of interplanetary space. Despite this, the model is still perfectly capable of fitting for the best orbital distribution per size bracket, and diagnosing the size-dependent trends of the meteoroid population:

$$N(a, e, i, H) = \sum_{s=1}^{n} \alpha_s(H) R_{s,t(H;\delta)}(a, e, i). \tag{C4}$$

The log-likelihood calculation uses a joint probability of a Poisson distribution, following the methods used in NEOMOD. For each bin j, the joint probability P of predicting n_j objects from the binned model output $N(a, e, i, H)$, for the number of expected objects λ_j in the debiased dataset $N_{\rm GFO}(a, e, i, H)$, is

$$P = \prod_j = \frac{\lambda_j^{n_j} \exp(-\lambda_j)}{n_j!}. \tag{C5}$$

The log-likelihood is therefore

$$\mathcal{L} = \ln P = -\sum_j \lambda_j + \sum_j n_j \ln \lambda_j, \tag{C6}$$

where the first term is the same for every model run, and the second term is evaluated only over nonzero bins: $n_j \neq 0$ and $\lambda_j \neq 0$. We also adopt the same prior function used in NEOMOD for our $\alpha_{s,m+1}$ to facilitate the constraint that they are not independent priors and must sum to 1 following Equation (C2). For sources $s = 1$ to $s = n - 1$, uniformly random parameters X_s are generated and transformed using

$$\alpha_{s,m+1} = [1 - (1 - X_s)^{1/(n-s)}]\left(1 - \sum_{k=1}^{s-1} \alpha_{k,m+1}\right) \tag{C7}$$

and

$$\alpha_{n,m+1} = 1 - \sum_{k=1}^{n-1} \alpha_{k,m+1}. \tag{C8}$$

This ensures Equation (C2) is fulfilled and `multinest` fits each α independently. The prior for the crossover parameter, δ, is uniform over the H-axis (Table 1). It ranges between 34.625 and 41.375, constrained to increments of 0.25 (H-axis bin width). Both $N(a, e, i, H)$ and $N_{\rm GFO}(a, e, i, H)$ are given to `multinest` along with the log-likelihood and prior functions to find the maximum log-likelihood between the two distributions. `multinest` is a Bayesian inference technique sampler (F. Feroz et al. 2019), and we specifically used the Python interface `PyMultiNest` (J. Buchner et al. 2014). The parameters α and δ are free parameters given to `multinest`, whereas n, s, m, and t are chosen before running a model fit. The number of parameters `multinest` fits for is therefore $n \times (m + 1) + 1$.

Appendix D
Results: Marginal Posterior Distributions

The parameter fitting by `multinest` produced marginal posterior distributions, which are shown for all parameters in Figure 11.

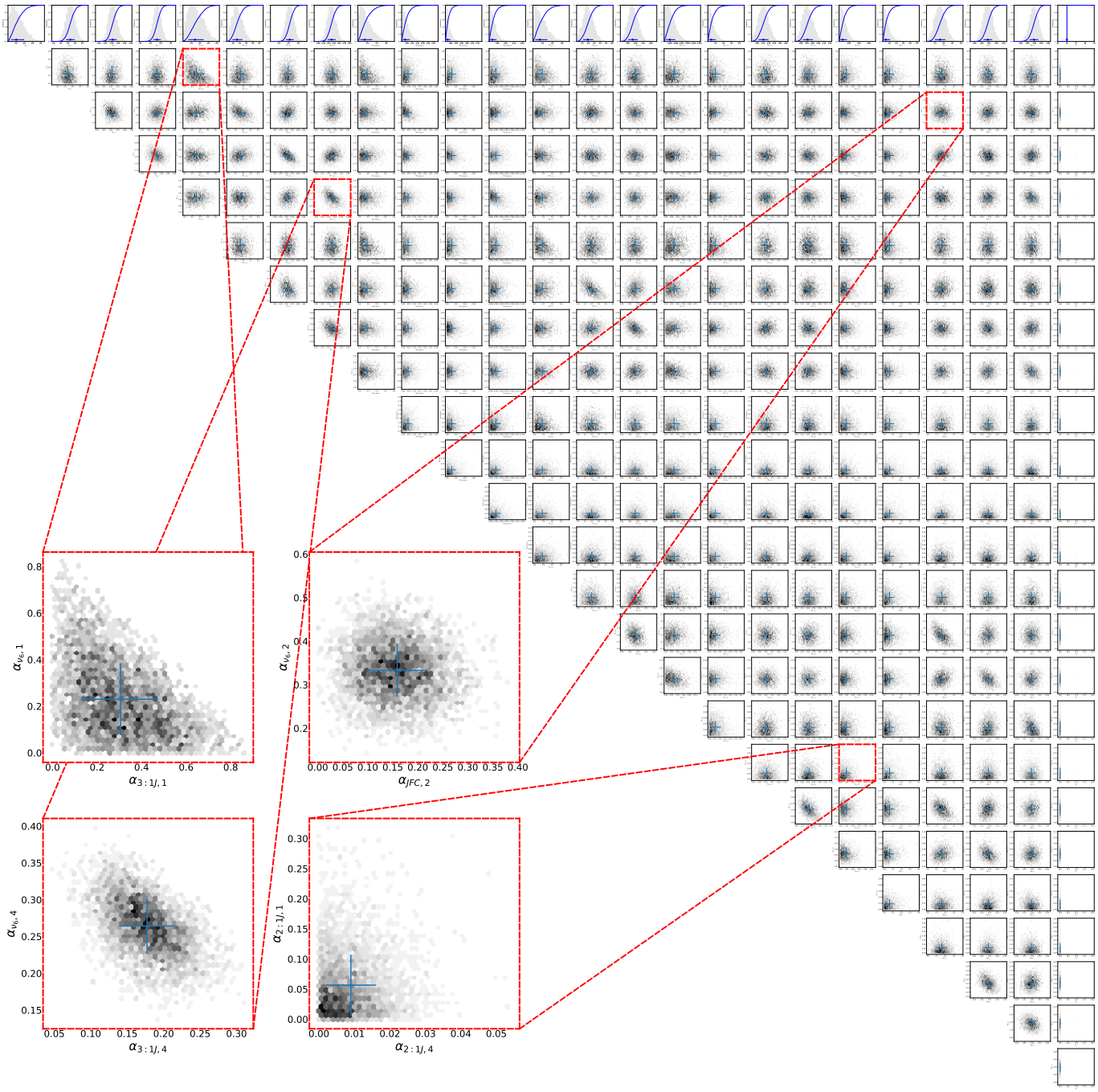

Figure 11. The marginal posterior distributions for the best-fitting model from `multinest`. It contains the sources for the inner weak resonances, ν_6, 3:1J, 5:2J, 2:1J, and JFCs. The zoomed insets show four examples of posterior distributions: major degeneracy (top left), well constrained (top right), minor degeneracy (bottom left), and low-to-zero contribution (bottom right). At the largest sizes of the model, the parameter $\alpha_I(H = 34.5)$ for the inner weak, ν_6, 3:1J, and 5:2J sources all show major degeneracy between them. Other minor degeneracies are seen between numerous sources (e.g., $\alpha_{\nu_6,4}$ and $\alpha_{3:1J,4}$). The crossover parameter, restricted to integer values, on the rightmost column shows significant preference for an index of 16 ($H = 38.5$).

Appendix E
Testing Model Stability

To investigate the stability of the model fit and ensure the results are not specific to any single meteoroid in the calibration dataset, we fit the model to half the dataset at a time. The data were randomly split into two subsets, A and B, and the model then fit. The $N_{\rm GFO}(a, e, i)$ was normalized to 601 instead of 1202 after weighting. Figure 12 shows that the general trends are consistent between subsets A and B; ν_6 is consistent, and the inner weak, 2:1J, and 5:2J resonances have minimal and decreasing contributions. The ratio of 3:1J and the JFC uptick with decreasing size is not consistent. This model is working with a small amount of data, so this is not unexpected.

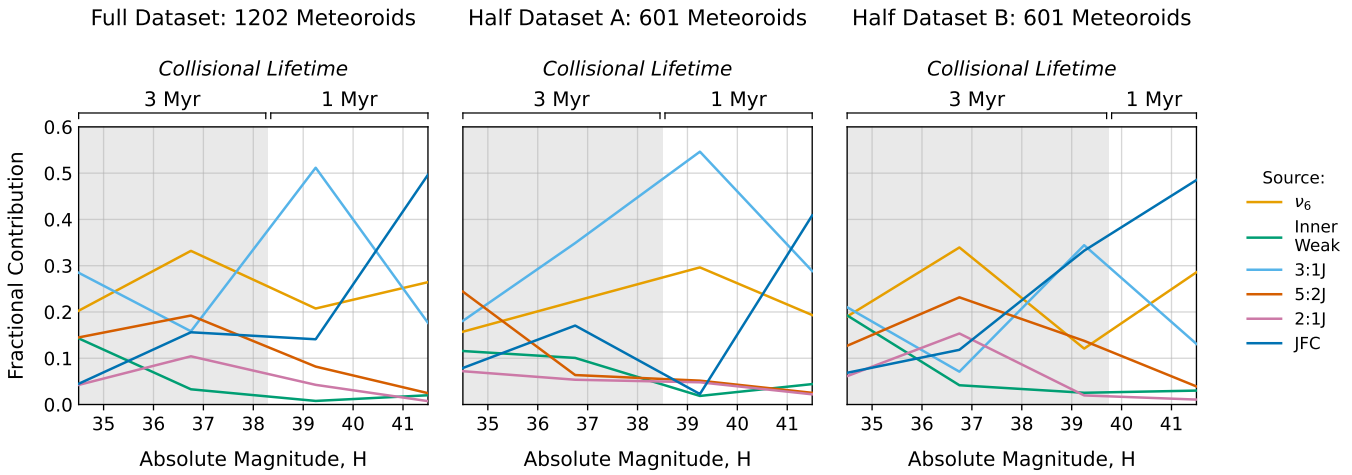

Figure 12. The median α parameters output from `multinest` for both the full dataset and half datasets A and B. The uncertainty bands for the half datasets are slightly wider than the full dataset (plotted in Figure 5) but omitted here for clarity. The crossover indices for the models run on datasets A and B are $H = 38.5$ ($\sim$0.6 kg) and $H = 39.75$ ($\sim$0.1 kg), respectively.

Appendix F
Identifying the Meteorite-dropping Population

We used several criteria to identify which fireballs captured by the GFO likely resulted in a meteorite falling to the ground. The fireball must have exhibited significant ($\geqslant$80%) overall deceleration and have fallen within the "likely dropper" parameter space of E. K. Sansom et al. (2019). These criteria identify events by their deceleration profile, specifically $\ln(\beta) \leqslant \ln(4.4 - \ln(\alpha\sin(\gamma)))$ for the mass loss and ablation parameters α and β and slope of entry γ. It is worth noting that these criteria were used generally for the entire dataset and do not take into account individual circumstances, which would be certainly be considered when determining whether any particular even did in fact drop a meteorite.

ORCID iDs

Sophie E. Deam https://orcid.org/0000-0003-1955-628X
Hadrien A. R. Devillepoix https://orcid.org/0000-0001-9226-1870
David Nesvorný https://orcid.org/0000-0002-4547-4301
Patrick M. Shober https://orcid.org/0000-0003-4766-2098
Eleanor K. Sansom https://orcid.org/0000-0003-2702-673X
Zouhair Benkhaldoun https://orcid.org/0000-0001-6285-9847
Peter G. Brown https://orcid.org/0000-0001-6130-7039
Luke Daly https://orcid.org/0000-0002-7150-4092
Hasnaa Chennaoui Aoudjehane https://orcid.org/0000-0001-8792-246X
Christopher D. K. Herd https://orcid.org/0000-0001-5210-4002
Jonathan Horner https://orcid.org/0000-0002-1160-7970
Peter Jenniskens https://orcid.org/0000-0003-4735-225X
Martin D. Suttle https://orcid.org/0000-0001-7165-2215
Anna Zappatini https://orcid.org/0000-0002-3020-4296

References

Battle, A., Reddy, V., Sanchez, J. A., et al. 2025, PSJ, 6, 31
Binzel, R. P., DeMeo, F. E., Turtelboom, E. V., et al. 2019, Icar, 324, 41
Binzel, R. P., Reddy, V., & Dunn, T. L. 2015, in Asteroids IV, ed. P. Michel, F. E. DeMeo, & W. F. Bottke (Univ. Arizona Press), 243
Bischoff, A., Patzek, M., Barrat, J.-A., et al. 2024, M&PS, 59, 2660
Bland, P. A., Spurný, P., Bevan, A. W. R., et al. 2012, AuJES, 59, 177
Boehnhardt, H. 2004, in Comets II, ed. M. C. Festou, H U. Keller, & H. A. Weaver (Univ. Arizona Press), 301
Borovička, J. 1990, BAICz, 41, 391
Borovička, J., Chesley, S. R., et al. 2016, IAUS, 318, 80
Borovička, J., Spurný, P., & Brown, P. 2015, Asteroids IV (Univ. Arizona Press), 257
Borovička, J., Spurný, P., Brown, P., et al. 2013, Natur, 503, 235
Borovička, J., Spurný, P., & Koten, P. 2007, A&A, 473, 661
Borovička, J., Spurný, P., & Shrbený, L. 2022, A&A, 667, A158
Boslough, M. B. E., & Crawford, D. A. 2008, IJIE, 35, 1441
Bottke, W. F., Durda, D. D., Nesvorný, D., et al. 2005a, Icar, 175, 111
Bottke, W. F., Durda, D. D., Nesvorný, D., et al. 2005b, Icar, 179, 63
Bottke, W. F., Meyer, A. J., Vokrouhlický, D., et al. 2025c, PSJ, 6, 150
Bottke, W. F., Morbidelli, A., Jedicke, R., et al. 2002a, Icar, 156, 399
Bottke, W. F., Jr., Vokrouhlický, D., Rubincam, D. P., & Broz, M. 2002b, in Asteroids III, ed. W. F. Bottke et al. (Univ. Arizona Press), 395
Bottke, W. F., Jr., Vokrouhlický, D., Rubincam, D. P., & Nesvorný, D. 2006, AREPS, 34, 157
Brož, M., Vernazza, P., Marsset, M., et al. 2024a, Natur, 634, 566
Brož, M., Vernazza, P., Marsset, M., et al. 2024b, A&A, 689, A183
Brown, P., Spalding, R. E., ReVelle, D. O., Tagliaferri, E., & Worden, S. P. 2002, Natur, 420, 294
Brown, P., Wiegert, P., Clark, D., & Tagliaferri, E. 2016, Icar, 266, 96
Brown, P. G., Assink, J. D., Astiz, L., et al. 2013, Natur, 503, 238
Buchner, J., Georgakakis, A., Nandra, K., et al. 2014, A&A, 564, A125
Burbine, T. H., & O'Brien, K. M. 2004, MAPS, 39, 667
Bus, S. J., & Binzel, R. P. 2002, Icar, 158, 146
Campbell-Brown, M. D. 2008, Icar, 196, 144
Ceplecha, Z., Borovička, J., Elford, W. G., et al. 1998, SSRv, 84, 327
Chow, I., & Brown, P. G. 2025, Icar, 429, 116444
Colas, F., Zanda, B., Bouley, S., et al. 2020, A&A, 644, A53
Ćuk, M., Gladman, B. J., & Nesvorný, D. 2014, Icar, 239, 154
de Elía, G. C., & Brunini, A. 2007, A&A, 466, 1159
Deam, S. E., & Nesvorny, D. 2025, Sampling and querying code for the Near-Earth Object Model Calibrated to Earth Impactors, v1.0, Zenodo, doi:10.5281/zenodo.17809512
Deienno, R., Denneau, L., Nesvorný, D., et al. 2025, Icar, 425, 116316
Delbo, M., Walsh, K. J., Matonti, C., et al. 2022, NatGe, 15, 453
DeMeo, F. E., Burt, B. J., Marsset, M., et al. 2022, Icar, 380, 114971
DeMeo, F. E., & Carry, B. 2013, Icar, 226, 723
DeMeo, F. E., & Carry, B. 2014, Natur, 505, 629
Devillepoix, H. A. R., Cupák, M., Bland, P. A., et al. 2020, P&SS, 191, 105036
Devillepoix, H. A. R., Sansom, E. K., Bland, P. A., et al. 2018, MAPS, 53, 2212
Di Sisto, R. P., Fernández, J. A., & Brunini, A. 2009, Icar, 203, 140
Dohnanyi, J. S. 1969, JGR, 74, 2531
Duncan, M., Levison, H., & Dones, L. 2004, in Comets II, ed. M. C. Festou, H. U. Keller, & H. A. Weaver (Univ. Arizona Press), 193
Duncan, M., Quinn, T., & Tremaine, S. 1988, ApJL, 328, L69

Duncan, M. J., & Levison, H. F. 1997, Sci, 276, 1670
Durda, D. D., Greenberg, R., & Jedicke, R. 1998, Icar, 135, 431
Egal, A., Vida, D., Colas, F., et al. 2025, NatAs, 9, 1624
Eugster, O. 2003, ChEG, 63, 3
Farinella, P., Vokrouhlický, D., & Hartmann, W. K. 1998, Icar, 132, 378
Farnocchia, D., Chesley, S. R., Brown, P. G., & Chodas, P. W. 2016, Icar, 274, 327
Fernández, J. A. 1980, MNRAS, 192, 481
Fernández, J. A., Gallardo, T., & Brunini, A. 2002, Icar, 159, 358
Fernández, J. A., & Sosa, A. 2015, P&SS, 118, 14
Fernández, Y. R. 2009, P&SS, 57, 1218
Feroz, F., Hobson, M. P., Cameron, E., & Pettitt, A. N. 2019, OJAp, 2, 10
Fuentes-Muñoz, O., Scheeres, D. J., Farnocchia, D., & Park, R. S. 2023, AJ, 166, 10
Gaffey, M. J., Reed, K. L., & Kelley, M. S. 1992, Icar, 100, 95
Galligan, D. P. 2001, MNRAS, 327, 623
Galligan, D. P., & Baggaley, W. J. 2005, MNRAS, 359, 551
Geng, S., Zhou, B., & Li, M. 2023, A&A, 670, A27
Gi, N., Brown, P., & Aftosmis, M. 2018, MAPS, 53, 1413
Gianotto, F., Carbognani, A., Fenucci, M., et al. 2025, Icar, 433, 116511
Gladman, B. J., Migliorini, F., Morbidelli, A., et al. 1997, Sci, 277, 197
Granvik, M., & Brown, P. 2018, Icar, 311, 271
Granvik, M., Morbidelli, A., Jedicke, R., et al. 2016, Natur, 530, 303
Granvik, M., Morbidelli, A., Jedicke, R., et al. 2018, Icar, 312, 181
Granvik, M., Morbidelli, A., Vokrouhlický, D., et al. 2017, A&A, 598, A52
Granvik, M., & Walsh, K. J. 2024, ApJL, 960, L9
Greenstreet, S., Ngo, H., & Gladman, B. 2012, Icar, 217, 355
Hajduková, M., Rudawska, R., Jopek, T. J., et al. 2023, A&A, 671, A155
Halliday, I., Griffin, A. A., & Blackwell, A. T. 1996, M&PS, 31, 185
Harris, A. W., & Chodas, P. W. 2021, Icar, 365, 114452
Harris, C. R., Millman, K. J., van der Walt, S. J., et al. 2020, Natur, 585, 357
Horner, J., Evans, N. W., & Bailey, M. E. 2004, MNRAS, 354, 798
Horner, J., Kane, S. R., Marshall, J. P., et al. 2020, PASP, 132, 102001
Howie, R. M., Paxman, J., Bland, P. A., et al. 2017a, ExA, 43, 237
Howie, R. M., Paxman, J., Bland, P. A., et al. 2017b, M&PS, 52, 1669
Hsieh, H. H., & Haghighipour, N. 2016, Icar, 277, 19
Hsieh, H. H., Novaković, B., Walsh, K. J., & Schörghofer, N. 2020, AJ, 159, 179
Hunter, J. D. 2007, CSE, 9, 90
Ingebretsen, C., Bolin, B. T., Jedicke, R., et al. 2025, AJ, 170, 237
Jansen-Sturgeon, T., Sansom, E. K., & Bland, P. A. 2019, M&PS, 54, 2149
Jenniskens, P. 2008a, EM&P, 102, 505
Jenniskens, P. 2008b, Icar, 194, 13
Jenniskens, P., & Devillepoix, H. A. R. 2025, M&PS, 60, 928
Jenniskens, P., Gabadirwe, M., Yin, Q.-Z., et al. 2021, M&PS, 56, 844
Jenniskens, P., Nénon, Q., Gural, P. S., et al. 2016, Icar, 266, 384
Jenniskens, P., Pilorz, S., Gural, P. S., et al. 2024, Icar, 415, 116034
Jenniskens, P., Shaddad, M. H., Numan, D., et al. 2009, Natur, 458, 485
Jewitt, D. 2012, AJ, 143, 66
Kareta, T., Vida, D., Micheli, M., et al. 2024, PSJ, 5, 253
Kim, Y., Ishiguro, M., & Usui, F. 2014, ApJ, 789, 151
King, A. J., Daly, L., Rowe, J., et al. 2022, SciA, 8, eabq3925
Kurlander, J. A., Bernardinelli, P. H., Schwamb, M. E., et al. 2025, AJ, 170, 99
Lemaitre, A. 1994, ASPC, 63, 140
Levison, H. F., & Duncan, M. J. 1994, Icar, 108, 18
Levison, H. F., & Duncan, M. J. 1997, Icar, 127, 13
Lucas, M. P., Emery, J. P., Pinilla-Alonso, N., Lindsay, S. S., & Lorenzi, V. 2017, Icar, 291, 268
Lue, A., Ruprecht, J. D., Varey, J., Czerwinski, M., & Viggh, H. E. M. 2019, Icar, 325, 105
Macke, R. J., Britt, D. T., & Consolmagno, G. J. 2011, M&PS, 46, 311
Mainzer, A. K., Masiero, J. R., Abell, P. A., et al. 2023, PSJ, 4, 224
Marsset, M., DeMeo, F. E., Burt, B., et al. 2022, AJ, 163, 165
Marsset, M., Vernazza, P., Brož, M., et al. 2024, Natur, 634, 561
Marti, K., & Graf, T. 1992, AREPS, 20, 221
Marty, B., Bermingham, K. R., Nittler, L. R., & Raymond, S. N. 2024, in Comets III, ed. K. J. Meech (Univ. Arizona Press), 681
McGraw, A., Reddy, V., & Sanchez, J. A. 2025, MNRAS, 537, 3145
Molaro, J., Walsh, K., Jawin, E., et al. 2020, NatCo, 11, 2913
Moorhead, A. V. 2016, MNRAS, 455, 4329
Morbidelli, A., & Gladman, B. 1998, M&PS, 33, 999
Morbidelli, A., & Vokrouhlický, D. 2003, Icar, 163, 120
Nesvorný, D., Deienno, R., Bottke, W. F., et al. 2023, AJ, 166, 55
Nesvorný, D., Janches, D., Vokrouhlický, D., et al. 2011, ApJ, 743, 129
Nesvorný, D., Jenniskens, P., Levison, H. F., et al. 2010, ApJ, 713, 816
Nesvorný, D., Roig, F., Vokrouhlický, D., & Brož, M. 2024a, ApJS, 274, 2
Nesvorný, D., Vokrouhlický, D., Bottke, W. F., & Sykes, M. 2006, Icar, 181, 107
Nesvorný, D., Vokrouhlický, D., Dones, L., et al. 2017, ApJ, 845, 27
Nesvorný, D., Vokrouhlický, D., Shelly, F., et al. 2024b, Icar, 411, 115922
Nesvorný, D., Vokrouhlický, D., Shelly, F., et al. 2024c, Icar, 417, 116110
O'Brien, D. P., & Greenberg, R. 2003, Icar, 164, 334
Öpik, E. J. 1951, PRIA, 54, 165
Piani, L., Marrocchi, Y., Rigaudier, T., et al. 2020, Sci, 369, 1110
Pokorný, P., Moorhead, A. V., Kuchner, M. J., Szalay, J. R., & Malaspina, D. M. 2024, PSJ, 5, 82
Pokorný, P., & Vokrouhlický, D. 2013, Icar, 226, 682
Popova, O. P., Jenniskens, P., Emel'yanenko, V., et al. 2013, Sci, 342, 1069
Rein, H., & Liu, S. F. 2012, A&A, 537, A128
Rein, H., & Spiegel, D. S. 2015, MNRAS, 446, 1424
Revelle, D. O., & Ceplecha, Z. 2001, ESASP, 495, 507
Rigley, J. K., & Wyatt, M. C. 2022, MNRAS, 510, 834
Ryabova, G. O., Asher, D. J., & Campbell-Brown, M. D. 2019, Meteoroids: Sources of Meteors on Earth and Beyond (Cambridge Univ. Press)
Sanchez, J. A., Reddy, V., Thirouin, A., et al. 2024, PSJ, 5, 131
Sansom, E. K., Bland, P., Paxman, J., & Towner, M. 2015, M&PS, 50, 1423
Sansom, E. K., Gritsevich, M., Devillepoix, H. A. R., et al. 2019, ApJ, 885, 115
Schunová, E., Jedicke, R., Walsh, K. J., et al. 2014, Icar, 238, 156
Shober, P. M. 2025, A&A, 702, A36
Shober, P. M., Courtot, A., & Vaubaillon, J. 2025a, A&A, 693, A23
Shober, P. M., Devillepoix, H. A. R., Vaubaillon, J., et al. 2025b, NatAs, 9, 799
Shober, P. M., Jansen-Sturgeon, T., Bland, P. A., et al. 2020, MNRAS, 498, 5240
Shober, P. M., Sansom, E. K., Bland, P. A., et al. 2021, PSJ, 2, 98
Shober, P. M., Tancredi, G., Vaubaillon, J., et al. 2024, A&A, 687, A181
Shustov, B. M., Naroenkov, S. A., & Efremova, E. V. 2017, SoSyR, 51, 38
Silber, E. A., Boslough, M., Hocking, W. K., Gritsevich, M., & Whitaker, R. W. 2018, AdSpR, 62, 489
Simion, N., Popescu, M., Licandro, J., et al. 2021, MNRAS, 508, 1128
Soja, R. H., Grün, E., Strub, P., et al. 2019, A&A, 628, A109
Southworth, R. B., & Hawkins, G. S. 1963, SCoA, 7, 261
Spoto, F., Milani, A., & Knežević, Z. 2015, Icar, 257, 275
Spurný, P., Borovička, J., Shrbený, L., Hankey, M., & Neubert, R. 2024, A&A, 686, A67
Svetsov, V., Shuvalov, V., Collins, G., & Popova, O. 2019, in Meteoroids: Sources of Meteors on Earth and Beyond, ed. G. O. Ryabova, D. J. Asher, & M. D. Campbell-Brown (Cambridge Univ. Press), 275
Tancredi, G. 1995, A&A, 299, 288
The pandas development team 2025, pandas-dev/pandas: Pandas, v3.0.0rc0, Zenodo, doi:10.5281/zenodo.17806077
Toliou, A., Granvik, M., & Tsirvoulis, G. 2021, MNRAS, 506, 3301
Towner, M. C., Cupak, M., Deshayes, J., et al. 2020, PASA, 37, e008
Usui, F., Kasuga, T., Hasegawa, S., et al. 2013, ApJ, 762, 56
Valsecchi, G. B., Jopek, T. J., & Froeschle, C. 1999, MNRAS, 304, 743
Vida, D., Šegon, D., Gural, P. S., et al. 2021, MNRAS, 506, 5046
Virtanen, P., Gommers, R., Oliphant, T. E., et al. 2020, NatMe, 17, 261
Vojáček, V., Borovička, J., Koten, J., Spurný, P., & Štork, P. 2015, A&A, 580, A67
Vokrouhlický, D., Pokorný, P., & Nesvorný, D. 2012, Icar, 219, 150
Wetherill, G. W. 1985, Metic, 20, 1
Wiegert, P., Brown, P., Pokorný, P., et al. 2020, AJ, 159, 143
Williams, J. G. 1992, Icar, 96, 251
Wisdom, J. 2020, MAPS, 55, 766
Wiśniowski, T., & Rickman, H. 2013, AcA, 63, 293